Deep-Sea Research, 1976, Vol. 23, pp. 655 to 679. Pergamon Press. Printed in Great Britain.

Topographically generated eddies*

HERBERT E. HUPPERT† and KIRK BRYAN‡

(*Received* 7 *August* 1975; *revision received and paper accepted* 18 *December* 1975)

Abstract—The interaction between temporally varying currents and the bottom topography of the ocean is investigated by the numerical and analytic examination of the following simple model. The flow of an inviscid, stratified fluid is initiated from relative rest in a uniformly rotating system containing an isolated topographic feature. The evolution of the flow redistributes vorticity and temperature in such a way that relatively cold water with anticyclonic vorticity exists over the topographic feature, while water shed from above the topographic feature sinks, thereby inducing a warm anomaly with cyclonic vorticity. For sufficiently strong oncoming flows, the shed fluid continually drifts downstream in the form of a relatively warm eddy. If the oncoming flow is relatively weak, the interaction between the anticyclonic and cyclonic vorticity distributions traps the warm eddy and it remains in the vicinity of the topographic feature.

We suggest that recent observations of an eddy in the vicinity of the Atlantis II Seamount and the existence of the large amount of high frequency energy near the bottom of the ocean measured by the MODE experiment may be partly explained in terms of the above mechanism. We conclude by speculating that vorticity redistribution by topography may be a contributing factor to cyclogenesis in the atmosphere.

1. INTRODUCTION

AS POSTULATED by STOMMEL (1955), a fascinating new view of oceanography arose when a set of pioneering measurements of deep currents was conducted in the late fifties and early sixties using neutrally-buoyant Swallow floats (SWALLOW and HAMON, 1960; CREASE, 1962; SWALLOW, 1971). These measurements were the first to indicate that the flow beneath the main thermocline is significantly variable in both space and time. In both the eastern and western North Atlantic the currents were found to vary on a time scale of a few weeks and a space scale of a few tens of kilometers. Many measurements confirming the significance of this temporal and spatial variability have been conducted since, the MODE experiment in an area 500 km by 400 km southwest of Bermuda being the latest (and most ambitious) program.

Explanations and prediction of the details of the variability are still being sought. Two physical mechanisms have received attention. One concept is that baroclinic instability occurs in the abyssal ocean to produce 'weather' in the main thermocline in a manner analogous to the generation of weather in the atmosphere. Theoretical calculations investigating this effect have been carried out by GILL, GREEN and SIMMONS (1974), ROBINSON and MCWILLIAMS (1974) and BRETHERTON (1975). The last two investigations imply that with parameters appropriate to the mid-Atlantic, models incorporating the effects of bottom topography induce baroclinic instabilities of sufficiently rapid growth-rate to be potentially important in mesoscale dynamics. The second mechanism to have received attention is the phenomenon of vortex ring formation by the Gulf Stream. PARKER (1971) studied approximately 200,000 bathythermograph records and identified 62 such rings, each of which drifted and slowly decayed over a period of at least 2 years. BRETHERTON (1975) argues from the results of numerical experiments by himself and those of RHINES (1975) that the most likely source of the small-scale noise which shows on the temperature and salinity sections all over the subtropical ocean basins is the offshore regions of the Gulf Stream and associated shedding of closed vortex rings.

Both of these explanations can be described in terms of eddies, a loosely defined concept implying temporal variability and rotational motion. Thus at any level the perturbation streamlines and associated isopycnals of an eddy field are closed curves evolving in time. Such a pattern is

*Contribution No. 44 from the Mid-Ocean Dynamics Experiment (MODE).

†Department of Applied Mathematics and Theoretical Physics, Silver Street, Cambridge, England.

‡Geophysical Fluid Dynamics Laboratory, NOAA, Princeton, N.J. 08540, U.S.A.

observed in everyday weather maps and occurred in the POLYGON and MODE experiments.

The aim of the present work is to investigate the interaction of variable mean currents with the bottom topography of the ocean. An outcome of our work is the generation of an eddy-like temperature and vorticity field by this interaction. Our work hence suggests an alternative method for the production of eddies in the deep ocean beneath the thermocline.

In order to build up an understanding of the features of the interaction of time-dependent mean currents with varying bottom topography, we investigate the following simplified model. A forced flow is initiated from relative rest in a rotating, stratified system to flow over an isolated topographic feature. Section 2 sets up the details of the model and presents a simplified physical explanation of the interaction, thereby building the framework which is added to in the following sections. Section 3 describes numerical investigations which yield the details of the interaction and confirm the validity of the physical framework of Section 2. The numerical results also yield a quantitative answer to the question of how much of the flow goes around and how much goes over the topographic feature. Section 4 presents a simplified analytic model which describes many of the aspects of the numerical results and hence can be used to predict details of the interaction for parameters different to those used in the numerical computations of Section 3. Section 5 summarizes the general results of our investigation and discusses some oceanographic data, taken in the New England Sea Mount Chain, which can be partly explained in terms of these results. The section continues with a few comments on the application of our results to the atmosphere and concludes with the observation that there are a large number of isolated topographic features in both the oceans and the atmosphere and these might be used to examine the applicability of the ideas contained in this work.

2. THE MODEL

In order to understand the essentials involved in the interaction of time-dependent flows and varying bottom topography, we consider the following situation as the simplest problem incorporating the desired effects. Inviscid, stratified fluid of mean depth H_0 and uniform buoyancy frequency N rotates about a vertical axis with constant angular velocity $\frac{1}{2}f$. The bottom boundary contains an isolated feature, of characteristic horizontal scale L, which is represented by $z = -H(x,y) \equiv h(x,y) - H_0$ in terms of the axes shown in Fig. 1. The fluid is at relative rest

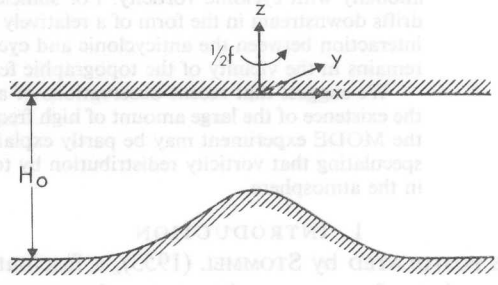

Fig. 1. A sketch depicting an isolated topographic feature and the co-ordinate system used in this paper.

initially and at $t = 0$ a pressure gradient in the y-direction is impressed on the system in such a way that there is a mean flow generated in the positive x-direction. Far upstream ($x = -\infty$) the flow approaches $U(t)$, a barotropic velocity independent of x, y or z, which monotonically increases in a time scale t_0 to the constant value U_0. We assume in this paper that t_0 is less than the advection time scale L/U_0, the time scale of the response to the initiation of the mean flow. The rotation of the system and the initiation of a mean current are the essential ingredients of the model and the aim of the investigation is to determine the temporal development of the resulting flow.

The first effect to occur is most easily explained in terms of the following framework. With reference to Fig. 2, as the mean flow is initiated, fluid originally at A is advected in a downstream direction to A′, vortex lines are compressed by the topography and anticyclonic vorticity is induced. This anticyclonic vorticity remains over the topographic feature to make up part of the final, large-time solution. Fluid originally at B is also advected downstream to B′, vortex lines

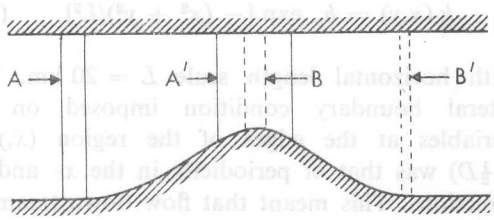

Fig. 2. A sketch of the initial, advective motion. The column of fluid at A is advected to A′ and that at B is advected to B′.

are stretched and cyclonic vorticity is induced. By Kelvin's circulation theorem, there is as much cyclonic vorticity generated as there is anticyclonic vorticity, and initially there is a fore–aft symmetry with the line joining the centers of the two vorticity distributions lying in the upstream–downstream direction. The time scale for this process is the advective time, L/U_0. As we discuss at greater length below, not all the fluid originally at A is advected *over* the isolated feature; some is advected *around* it. While this effect decreases the amount of anticyclonic vorticity induced, it does not alter the main qualitative features of the flow.

Subsequent to the advection phase, the flow is influenced by two effects. One, the vorticity distributions interact. This interaction tends to rotate the center of the cyclonic vorticity distribution around the trapped anticyclonic vorticity distribution. Two, the cyclonic vorticity is influenced by the oncoming flow which tends to advect it downstream. The combination of these two effects results in one of two very different flows. Either the movement of the cyclonic vorticity distribution is dominated by the oncoming flow, in which case the cyclonic vorticity distribution after some time drifts downstream, or the movement is dominated by the vorticity–vorticity interaction, in which case the cyclonic vorticity distribution is trapped by the anticyclonic vorticity and remains in the vicinity of the isolated topographic feature.

This discussion has been in terms of vorticity because of its dynamical prominence. In a stratified fluid the same discussion can be carried out in terms of density as follows. Relatively heavy fluid at the base of A is initially advected to the top of the topographic feature. Relatively lighter fluid, at the base of B, is advected off the feature. The relatively heavier fluid at the top of the feature is constantly replenished by the oncoming flow. The lighter fluid, initially on top of the feature, sinks and either drifts downstream as a relatively lighter patch of fluid or is forced by its interaction with the fluid above the topographic feature to remain close to it. We examine these two different types of flow and evaluate the parametric regions in which they occur by both numerical and analytical models below.

The large time, steady-state flow induced by relatively shallow features has been recently investigated analytically by HOGG (1973) for the special case of a right circular cylinder and by HUPPERT (1975) for more general topography. The latter calculates the flow field using quasi-geostrophic theory and shows that topographic features above a critical height induce regions of closed streamlines or Taylor columns. Below this critical height no closed streamlines occur. In this regime, the main feature of the flow is the comparatively larger velocity in the vicinity of the topography on the left looking downstream and an accompanying smaller velocity on the right. Huppert derives formulae yielding the critical height for circularly symmetric topographic features [equations (1) and (2) of his abstract] and presents numerical results appropriate to three different topographic shapes (his Fig. 3).

The major thrust of the present work is the investigation of time-dependent flows induced by features sufficiently large that Huppert's steady-state solutions indicate that there is a region of closed streamlines in the flow, and his results represent a useful foundation against which we can test our present numerical calculations and make a number of interesting comparisons.

3. THE NUMERICAL CALCULATIONS

Governing equations

The numerical calculations were performed using the equations of motion for a stratified fluid moving with respect to a uniformly rotating system. The Boussinesq approximation was

invoked and a hydrostatically balanced vertical pressure gradient was used. A small linear, horizontal diffusivity of heat and horizontal momentum was included for numerical purposes. Under the influence of only this diffusivity, a generated disturbance would decay in a time scale of over a hundred days. Hence the effect on the generation of the vorticity distribution and its initial movement is negligible.

Denoting the horizontal velocity vector by $\mathbf{q}$, the vertical component of the velocity by w and using the representative density ρ_0, we write the momentum equations as

$$\partial_t \mathbf{q} + \mathbf{q} \cdot \nabla \mathbf{q} + w\, \partial_z \mathbf{q} + f \hat{\mathbf{z}} \wedge \mathbf{q} = -\rho_0^{-1} \nabla p + A_H \nabla^2 \mathbf{q} \quad (3.1)$$

$$0 = -\partial_z p - \rho g, \quad (3.2)$$

and the equation of continuity as

$$\nabla \cdot \mathbf{q} + \partial_z w = 0, \quad (3.3)$$

where ∇ and ∇^2 are horizontal operators and A_H is the horizontal diffusivity discussed above. To these we add a linear equation of state relating temperature and density

$$\rho = \rho_0 (1 - \alpha T) \quad (3.4)$$

and the temperature conservation equation

$$\partial_t T + \mathbf{q} \cdot \nabla T + w\, \partial_z T = A_H \nabla^2 T. \quad (3.5)$$

The requirement of zero normal flow at the upper and lower boundaries stipulates that

$$w = 0 \qquad (z = 0) \quad (3.6)$$

and that

$$w = -\mathbf{q} \cdot \nabla H \qquad (z = -H). \quad (3.7)$$

Equations (3.1) to (3.7) were solved in a region of horizontal dimensions 245 by 245 km and depth $H_0 = 4$ km. The topographic feature in each calculation was a centrally-situated, circularly symmetric gaussian

$$h(x,y) = h_m \exp[-(x^2 + y^2)/L^2] \quad (3.8)$$

with horizontal length scale $L = 20$ km. The lateral boundary condition imposed on all variables at the edges of the region ($x,y = \pm\frac{1}{2}D$) was that of periodicity in the x- and y-directions. This meant that flow downstream of the topographic feature eventually reappeared upstream. The present work benefitted from this effect since it artificially increased the length of the downstream section.

The forcing of the flow was prescribed by imposing the constraint

$$\int_{-H}^{0} \int_{-\frac{1}{2}D}^{\frac{1}{2}D} \mathbf{q}\, dy\, dz = ULH_0\,(1, 0), \quad (3.9)$$

which implies that the total downstream transport is uniform and that there is no net drift in the cross-stream direction. Each numerical experiment started from a state of rest. At $t = 0$ the forced transport was slowly increased to its final value over a transition period of 1 day. Explicitly

$$U = 0 \qquad (t \leq 0) \quad (3.10)$$

$$U = U_0 \tanh(t/t_0) \quad (t \geq 0), \quad (3.11)$$

with t_0 equal to 1 day.

The neglect of bottom friction in our model requires some comment. The effect of including bottom friction would be to reduce both the cyclonic and anticyclonic vorticity generated. Over the feature, regions of closed streamlines will be spun down by Ekman suction. Away from the feature, the shed anomaly will be retarded in its movement and, due to the reduced anticyclonic vorticity, will be less affected by the vorticity–vorticity interaction. The influence of these effects on our results is dependent upon the magnitude of the bottom friction. Estimates of this quantity in the ocean vary enormously. Possibly the most comprehensive study undertaken is that of WEATHERLY (1972). His study in a typical region in the Straits of Florida indicates that a bottom stress of 0.2 dyne cm^{-2} was produced by

a mean external velocity of approximately 10 cm s^{-1}. Use of linear Ekman boundary layer theory suggests that the inclusion of a bottom stress τ in our model will decrease the magnitude of the generated vorticity by the fraction $[\tau N/(fU^2)]^2$. Even for a bottom stress an order of magnitude larger than the one indicated by Weatherly's study, this fraction is less than 5%, implying that we can safely neglect the effect of bottom friction.

Parameters

The calculations were carried out using the finite difference scheme described by BRYAN (1969) with some minor modifications. The numerical scheme used centered differences with respect to both time and space. The timestep used in the calculation varied from 86.4 steps day^{-1} for the slowest flows to 432 steps day^{-1} for the fastest flows. In the horizontal plane the finite difference mesh was uniform with a 5-km spacing between grid points. In the vertical the spacing varied smoothly but non-uniformly to allow for a more detailed resolution near the bottom than the top. A departure from the BRYAN (1969) scheme is that the lowest cells near the bottom can be of non-uniform thickness and the thickness of the lowest cell can be (and was) chosen to match the actual bottom configuration. This generalization permits the depth to vary smoothly from one mesh point to another without sacrificing the integral preserving properties of the model. Dependent on the maximum height of the topographic feature, one of two different sets of cell thicknesses were used. The depth of the centre point of each cell is tabulated in Table 1.

The parameters used in the numerical calculations can be divided into two categories. The first category consists of those parameters which were the same for all experiments. These parameters and their values are tabulated in Table 2. The second category consists of the two parameters U_0 and h_m which were varied from experiment to experiment. The value of U_0 was varied between 0.5 and 25 cm s^{-1} and the value of h_m between 75 and 800 m. Twelve calculations using different values of U_0 and h_m were performed, with each calculation continued for at least 3000 timesteps. The values of U_0 and h_m used in each calculation can be determined from Fig. 13b which presents a datum point from each experiment.

Table 1. Depth (in m) of the center point in each layer of the numerical model. Arrangement A and B were used for cases of moderate and large amplitude bottom topography, respectively.

Level	Arrangement A	B
1	400	293
2	1197	878
3	1980	1462
4	2715	2041
5	3325	2603
6	3720	3119
7	3903	3530
8	3967	3791
9	3991	3941

Table 2. The fixed parameters of the numerical calculations.

Parameter	Value	Description
L	20 km	Horizontal length scale of the topographic feature
H_0	4 km	Maximum depth
f	10^{-4} s^{-1}	Inertial frequency
N	10^{-3} s^{-1}	Buoyancy frequency
NH_0/fL	2	Stratification parameter
A_H	40 m^2 s^{-1}	Horizontal mixing coefficient

The time-dependent solutions

It was possible to test the numerical scheme by maintaining the flow over a low topographic feature for a long enough time that the flow settles down and then compare the results with HUPPERT's (1975) analytic calculations. As discussed in the previous section, a cyclonic vortex is formed during the initial stages of the flow which drifts downstream, leaving an isolated anticyclonic vortex over the feature. Due to the cyclic boundary

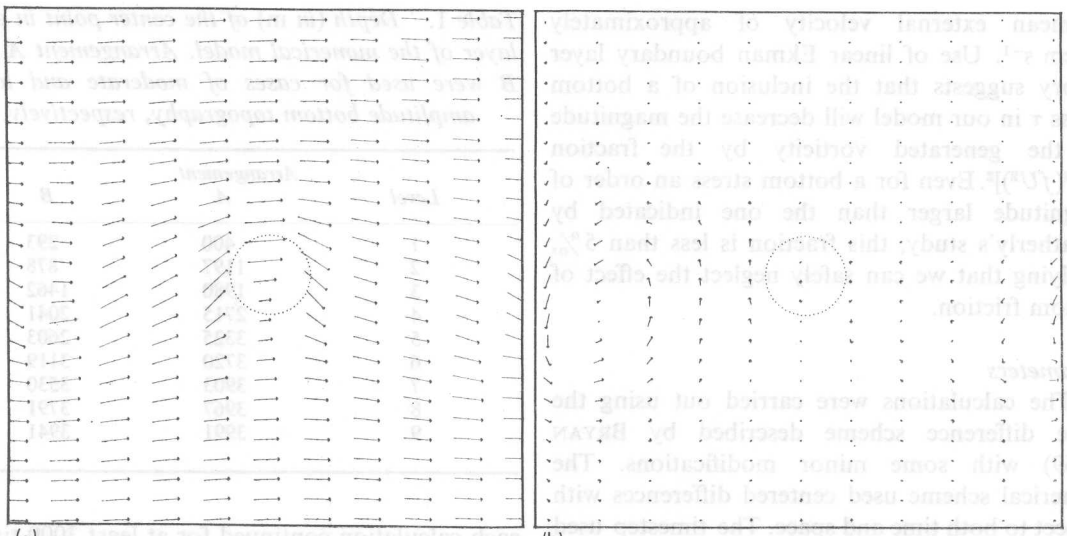

Fig. 3. The horizontal velocity vectors after 34.7 days at a depth of 3903 m for $U_0 = 5.1$ cm s^{-1} and $h_m = 75$ m. (a) The present numerical calculations. (b) The numerical calculations minus HUPPERT's (1975) analytic calculations. On this and subsequent figures the dotted circle represents a circle of radius 20 km, the length scale of the isolated topographic feature.

conditions employed in the numerical calculations, the drifting cyclonic vortex reappears upstream making it difficult to obtain a completely isolated anticyclonic vortex in the numerical model. This difficulty is circumvented by terminating the numerical integration before the drifting vortex moves into the near vicinity of the feature. Figure 3a presents the horizontal velocity vectors after 3000 timesteps (34.7 days) at level 7 (3903 m) for a calculation with $U_0 = 5.1$ cm s^{-1} and $h_m = 75$ m. In Fig. 3b the vector difference between HUPPERT's (1975) analytic solution and the numerical solution is shown. It is clear that there is good agreement between the two solutions except in the vicinity of the drifting cyclonic vorticity. A careful evaluation of the numerical results indicates that except in the vicinity of this cyclonic vorticity the difference between the two solutions is in the range of approximately 5 to 10%. This difference can be attributed to the fact that the analytic solution is derived for zero Rossby number and applies the lower boundary condition at $z = -H_0$ rather than $z = -H$, while the numerical solution includes a small truncation error. Considering these differences between the two models, the solutions are in good agreement and lend credence to the description given below.

The description of the details of a time-dependent, three-dimensional flow is not easy. The task is somewhat simplified by the fact that the qualitative features of the flow tend to be very coherent along a vertical coordinate with the density perturbation, $\Delta\rho$, attenuating with increasing distance above the bottom according to

$$\Delta\rho\,(x, y, z, t) = \Delta\rho\,(x, y, -H, t) \times \frac{\sinh\,(-Nz/fL)}{\sinh\,(NH/fL)}, \quad (3.12)$$

as indicated by HUPPERT's (1975) analytic theory. The validity of (3.12) is demonstrated for one particular situation ($U_0 = 5.1$cm s^{-1}, $h_m = 200$ m) in Fig. 4. Thus our description can concentrate on the level just above the top of the isolated feature and on the lower levels which intersect the feature.

Examining our results, we find that the patterns of the density and the linearly related

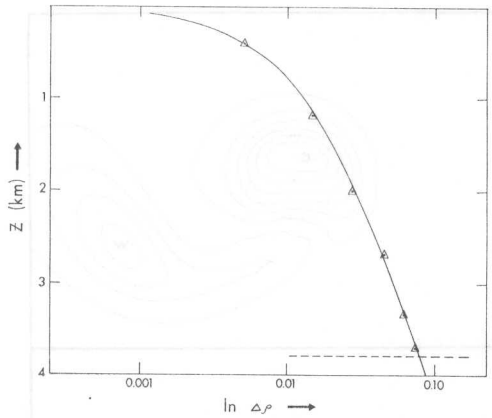

Fig. 4. The density perturbation at $x = y = 0$ after 34.7 days for $U_0 = 5.1$ cm s^{-1} and $h_m = 200$ m. The triangles (Δ) represent the results of the numerical calculations and the solid curve is given by $\Delta\rho\,(x, y, z, t) = \Delta\rho\,(x, y, t)\,\sinh\,(-Nz/fL)/\sinh\,(NH/fL)$.

temperature anomalies correspond very closely to those of vorticity, as we expect from previous theoretical calculations. Since oceanographers measure density or temperature rather than vorticity, we present most of the pictorial aspects of our results in terms of these variables. However, since vorticity is a twice differentiated property of the flow field, the smoothness of the vorticity field is a rather stringent test of the accuracy of the finite difference scheme. Hence we present a few vorticity figures, both to exhibit the similarity between the density anomalies and the vorticity field and to indicate the accuracy of our numerical calculations.

We present detailed results for two flows with $h_m = 200$ m. For the first case $U_0 = 5.1$ cm s^{-1}, herein case F (fast), and for the second case $U_0 = 1.0$ cm s^{-1}, herein case S (slow). For case F the shed vorticity drifts downstream, while for case S it remains near the topographic feature. We compare the temperature and vorticity patterns for these two cases level for level.

The evolution of the temperature pattern for case F at level 6 (3720 m), the first level above the top of the feature, is shown in Fig. 5. As the flow commences the response consists of an upwelling on the upstream side of the feature leading to a relatively cold patch of water over the feature and a downwelling on the lee side leading to a relatively warm patch of water downstream. This occurs in the advective time scale L/U_0. Thereafter the warm anomaly rotates clockwise around the feature and, under the influence of the oncoming stream, gradually elongates and eventually drifts downstream, leaving a long tail of warm water in its wake. Due to the periodic boundary conditions employed in the calculation the drifting warm anomaly reappears upstream after some 23 days (2000 timesteps). After 35 days the warm anomaly has spread out considerably and decreased 50% in amplitude. By contrast, the cold anomaly remains stationary, displaced slightly to the left of the feature, maintaining an approximately constant amplitude. Figure 6a shows the velocity vectors for this case and level at 35 days. These vectors are drawn at every fifth grid point in the x-direction and every other grid point in the y-direction. We see clearly that in the vicinity of the feature the fluid first moves to the left (looking downstream) around the feature and then turns sharply to the right after it has passed over it. To the right of the top of the feature there is a circular, nearly stagnant region approximately 25 km in diameter. Figures 7a, b present the vorticity for the same case and level after 7 days and 35 days, the same times as Figs. 5b, e. The similarity between the vorticity and temperature patterns is clearly evident.

We now consider the flow for case S at level 6. Initially the response is similar to that for case F except that a greater proportion of the flow goes around rather than over the feature, an effect to be discussed in detail below. The evolution of the temperature pattern is shown in Fig. 8. The distinctive feature in contrast to case F is the tendency of the cold and warm anomalies to be very tightly wrapped around each other. This tendency reaches a maximum after approximately 18 days. Thereafter the pattern loosens up somewhat but there is no indication that the warm anomaly drifts off downstream as for case F. The numerical calculation was continued for 70 days and confirmed this point. Figure 9 shows the vorticity pattern after 9 days; the similarity between this pattern and the temperature pattern in Fig. 8b is clear.

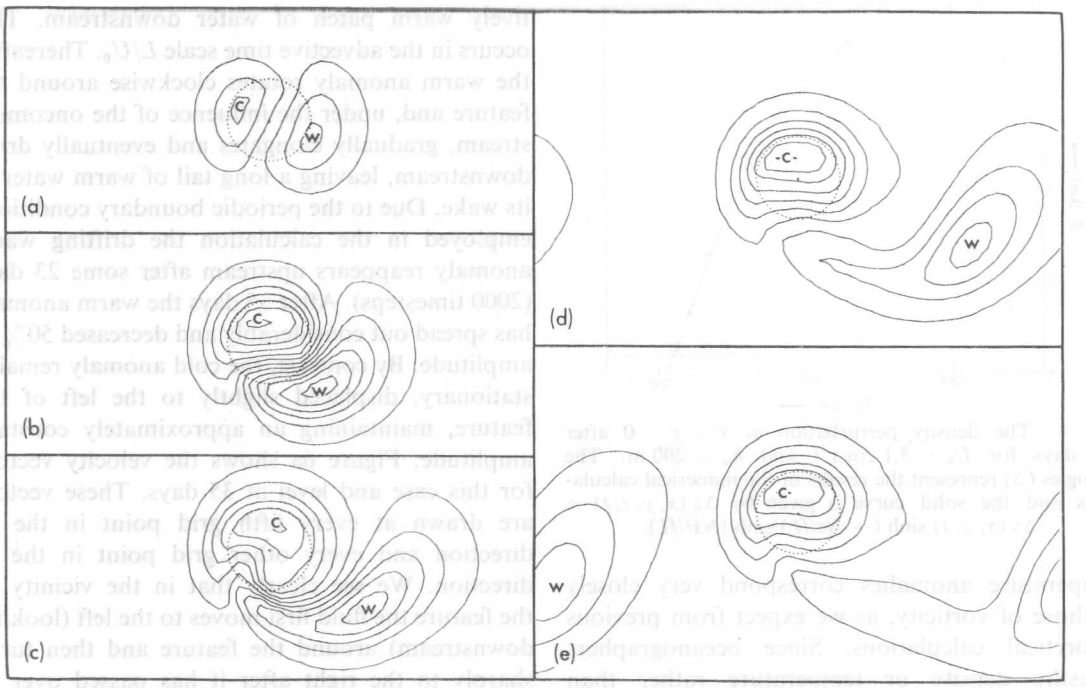

Fig. 5. The isopycnals with a contour interval of $\Delta\rho/\rho_0 = 16 \times 10^{-6}$ at a depth of 3720 m for $U_0 = 5.1$ cm s^{-1} and $h_m = 200$ m. (a) 2.3 days, (b) 6.9 days, (c) 13.9 days, (d) 23.1 days and (e) 34.7 days. In this and subsequent figures C marks the cold anomaly and W the warm anomaly. Note that much of the 245 × 245 km area contains very little density variation and to save space is not shown in this and subsequent figures.

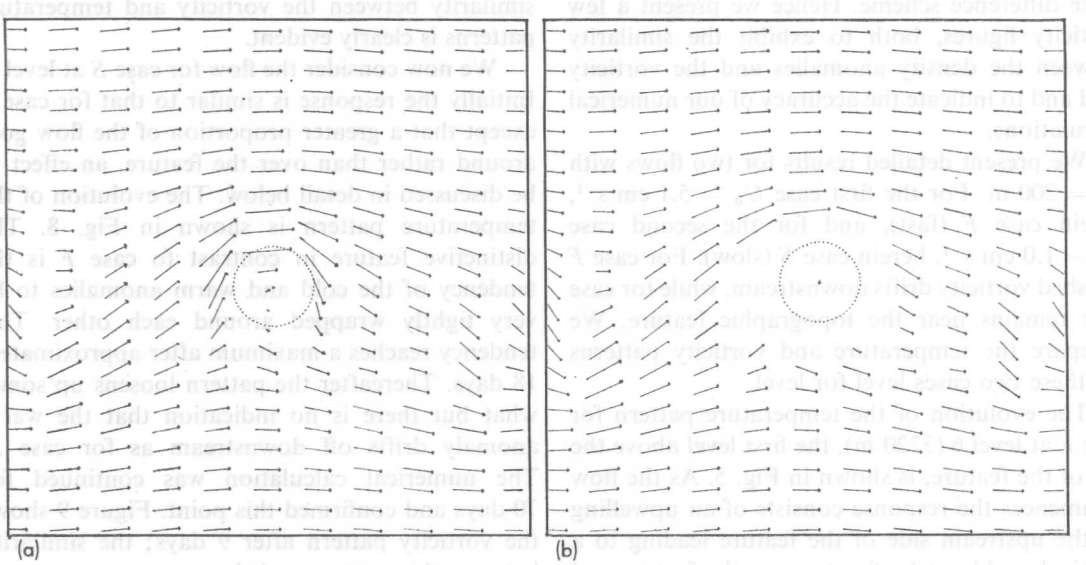

Fig. 6. The horizontal velocity vectors after 34.7 days for $U_0 = 5.1$ cm s^{-1} and $h_m = 200$ m. (a) At a depth of 3720 m. (b) At a depth of 3991 m.

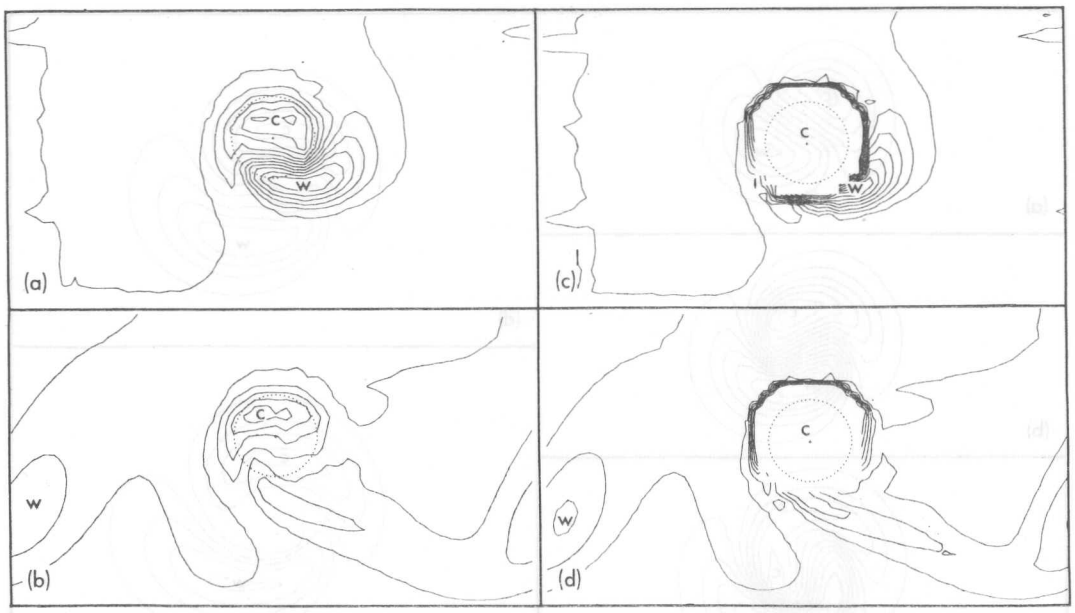

Fig. 7. The relative vorticity with a contour interval of $2{\cdot}0 \times 10^{-6}$ s^{-1} for $U_0 = 5.1$ cm s^{-1} and $h_m = 200$ m.

	Depth (m)	Time (days)
(a)	3720	6.9
(b)	3720	34.7
(c)	3967	6.9
(d)	3967	34.7

We now turn to describing the flow at a level intersecting the topographic feature. The evolution of the temperature pattern for case *F* at level 8 (3967 m) is shown in Fig. 10. The first pattern, after 2 days, depicts a very small thermal response: cold water just upstream of the feature has been replaced by water of the same temperature originally slightly further upstream and the relatively warmer water which has been displaced from the top of the feature has not yet reached the lower level. As time proceeds the influence of the warmer water does penetrate to this lower level and, in accordance with the warm anomalies at higher levels, the warm anomaly at this level rotates clockwise around the feature and then, continuously supplied by water moving downslope off the feature, it drifts off downstream, with a warm water wake. The line joining the centers of the drifting warm anomalies from level to level is almost vertical. Upstream of the feature, for the reason described above, the thermal response is small for all times. In particular, in the water at levels below the top of the feature there is not the trapped, relatively cold anomaly which appears above the feature. In Fig. 6b the velocity vectors at level 9 (3991 m) after 35 days are drawn. The general tendency of relatively rapid flow to the left of the feature is present, though to a smaller extent than at higher levels. Figures 7c and d show the vorticity patterns at level 8 at the same timesteps as the qualitatively similar temperature patterns in Figs. 10b and e.

Figure 11 shows the evolution of the temperature patterns for case *S* at level 8. Throughout the motion the horizontal temperature gradients are not as large as they are for case *F* at this level.

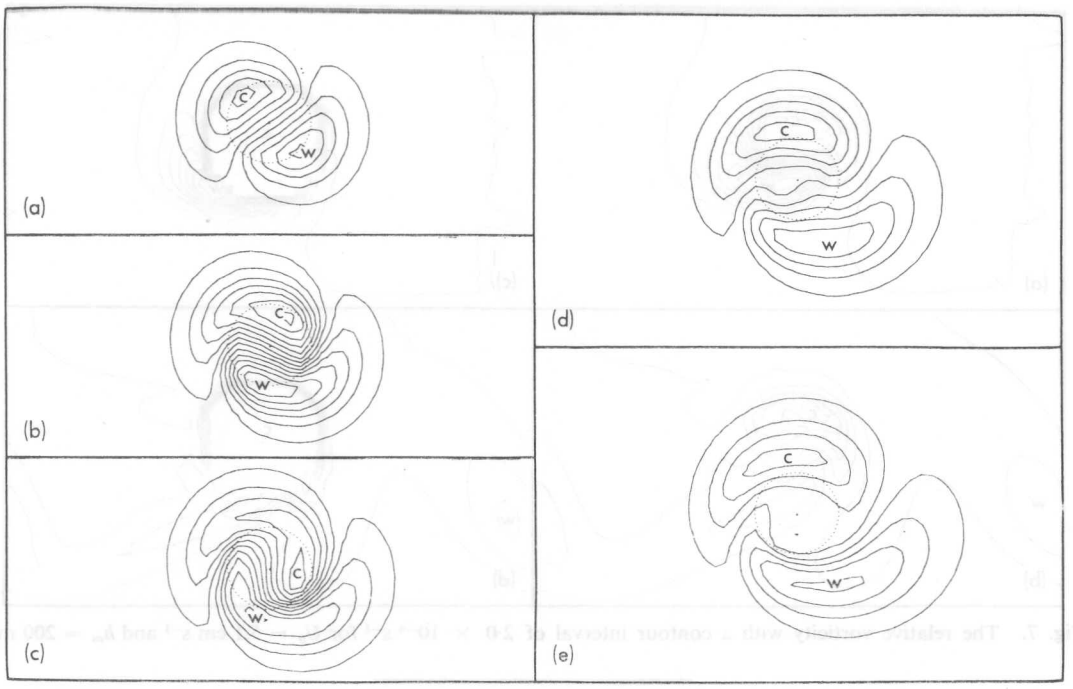

Fig. 8. The isopycnals with a contour interval of $\Delta\rho/\rho_0 = 4\times10^{-6}$ at a depth of 3720 m for $U_0 = 1.0$ cm s^{-1} and $h_m = 200$ m. (a) 4.6 days, (b) 9.3 days, (c) 13.9 days, (d) 23.1 days and (e) 34.7 days.

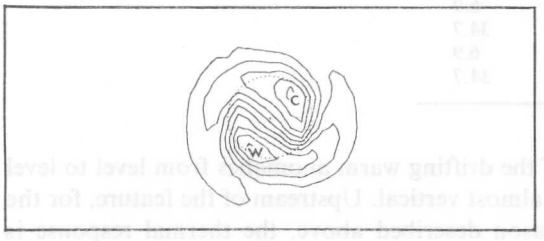

Fig. 9. The relative vorticity with a contour interval of 7.5×10^{-7} s^{-1} after 9.3 days at a depth of 3720 m for $U_0 = 1.0$ cm s^{-1} and $h_m = 200$ m.

There is no tendency for either the warm or cold anomaly to move away from the feature.

On comparing the magnitude of the temperature anomalies over the topographic feature in the F and S cases, it is clear that significantly less fluid flows over the feature in case S than in case F. The question of how much fluid flows over and how much flows around a particular topographic feature is a central, yet essentially unanswered question in the study of stratified flows over obstacles, in both non-rotating and rotating systems.* Not even a suitable quantitative parameter to be used in discussing the problem has even been suggested. There is some difficulty about this since while the idea expressed in the use of the words 'over' and 'around' is clear, how to quantify the idea is not clear. Even in homogeneous, non-rotating flows, where there is no restriction to oncoming fluid particles being lifted over an obstacle, most fluid particles originate off the upstream axis of the obstacle and to some extent they must go 'around' the obstacle. We suggest that a useful quantitative measure can be constructed as follows. Consider a horizontal plane touching the top of the obstacle. We now ask: what is the maximum (upward) vertical displacement a fluid particle has undergone in order to reach this plane? By non-dimensionalizing this displacement by the maximum height of the obstacle, we obtain a parameter,

*A noteworthy attempt to investigate this problem was carried out by DRAZIN (1961), but he considered only non-rotating systems in the limits of very small or very large stratification.

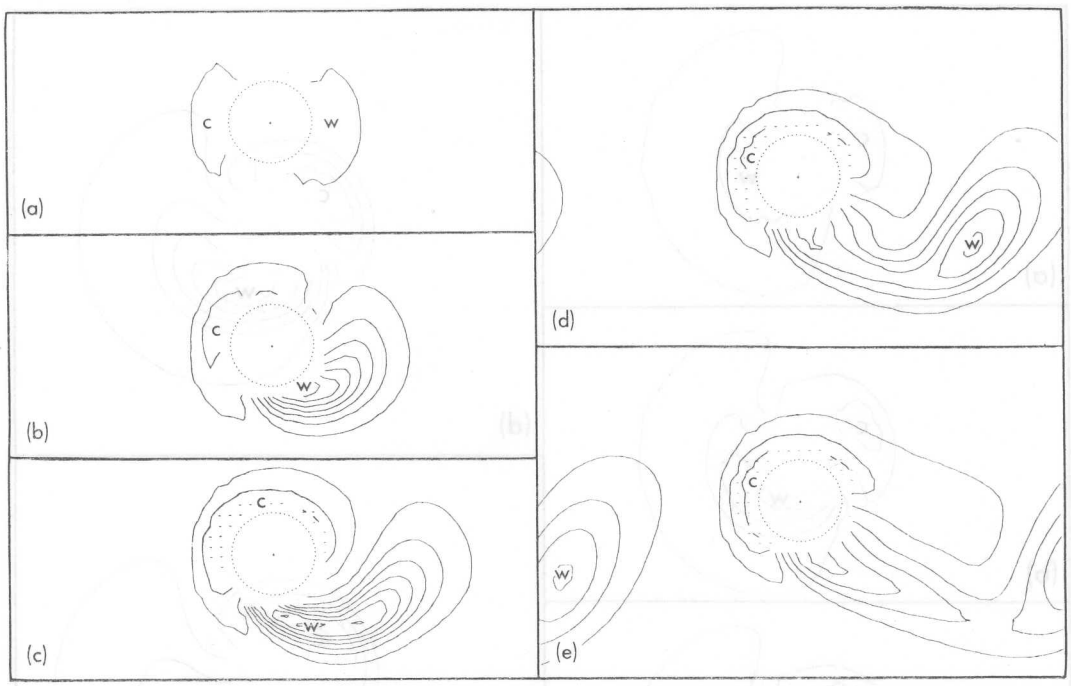

Fig. 10. The isopycnals for the same situation as in Fig. 5 except that the depth is 3967 m.

say δ, which ranges between 0 and 1. A zero value of δ means that the flow is completely inhibited from flowing over the obstacle: the fluid flows in solely horizontal planes (very strong stratification). A value of unity for δ means that at least some fluid rises to the height of the obstacle and, by our definition, there is no inhibition to flow 'over' the obstacle. Intermediate values of δ quantify partial inhibition to flow 'over' the obstacle. This concept could be generalized in a number of ways, including the consideration of horizontal planes at various depths intersecting the obstacle, or by the determination of the vertical displacement of either the particle at the top of the obstacle or the particle with minimum or maximum velocity, for example.

The vertical displacement undergone by a particle can be most easily determined by examining the temperature field and using the fact that to a very high degree of approximation the temperature of a particle is a conserved quantity. Thus the temperature at any point immediately yields the depth from which the particle originated. In accord with the description of the preceding paragraph, we have determined the point of minimum temperature in the horizontal plane at the first level above the top of the topographic feature (level 7 for $h_m = 75$ m and level 6 for $h_m =$ 200 m or 800 m) and thus evaluated the maximum vertical displacement. This procedure leads to the maximum vertical displacement at a plane in a height say d above the top of the feature. But since the disturbance decays with a vertical scale given by (3.12) as fL/N, which is very much greater than d, the results will be virtually identical with those obtained by interpolating the temperature field to a depth equal to the top of the feature. The non-dimensionalized displacements are graphed against the velocity non-dimensionalized by the critical velocity U_c in Fig. 12. The value of U_c is determined from HUPPERT's (1975) analysis as the velocity at which a closed streamline first appears in the flow. The data is well described by the relationship:

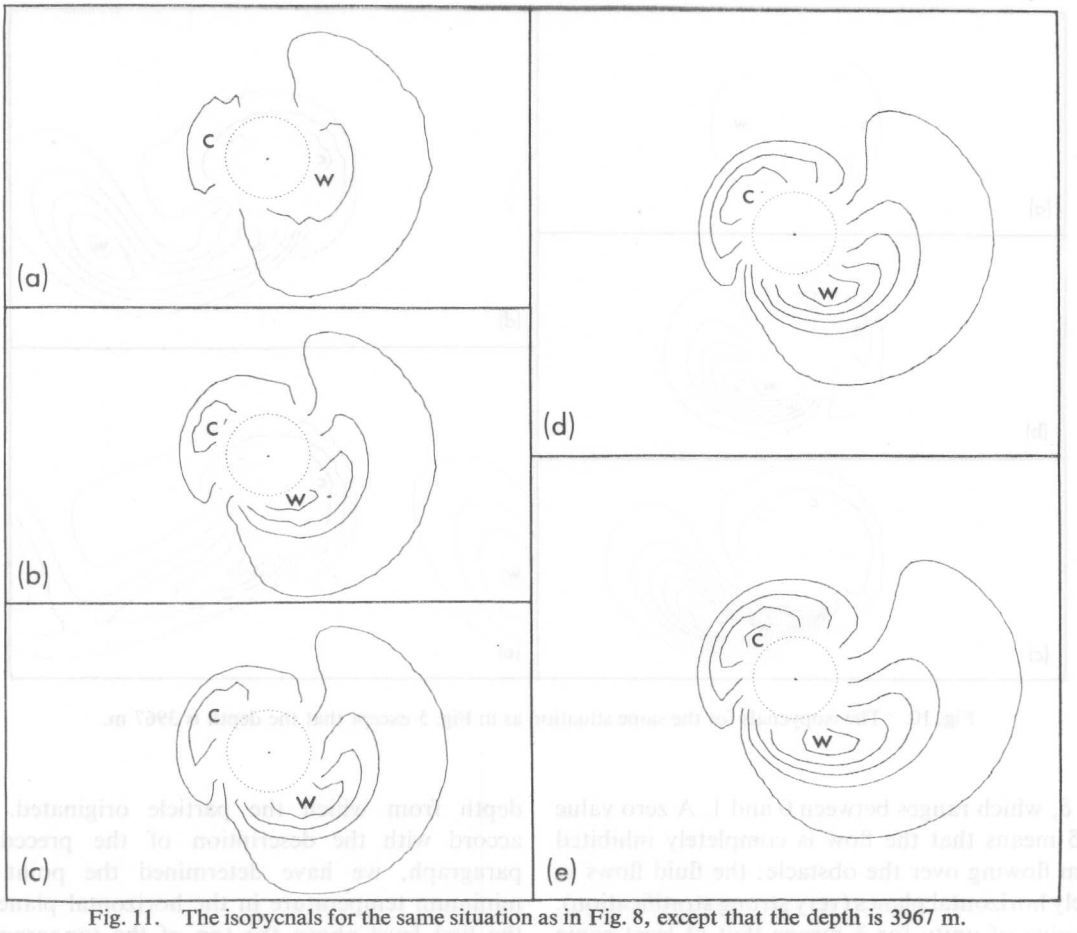

Fig. 11. The isopycnals for the same situation as in Fig. 8, except that the depth is 3967 m.

$$\delta = U_0/U_c \qquad (U_0 \leq U_c) \tag{3.13a}$$

$$= 1 \qquad (U_0 \geq U_c). \tag{3.13b}$$

An explanation of this relationship is as follows. For $U \geq U_c$, in the sense of the preceding paragraph all the flow goes over the feature and hence $\delta = 1$. For $U_0 < U_c$, on dimensional grounds

$$\delta = \frac{\delta^*}{h_m} = F_1\left(\frac{U_0}{Nh_m}, \frac{NH_0}{fL}, \frac{f}{N}, \frac{U_0}{fL}\right), \tag{3.14a,b}$$

where δ^* is the dimensional vertical displacement and F_1 is a non-dimensional function dependent on its four non-dimensional arguments and the shape of the topographic feature. Our results hold in the limit of small $U_0/(fL)$ and constant f/N and NH_0/fL so we can rewrite (3.14) as

$$\delta = \frac{\delta^*}{h_m} = F_2\left(\frac{U_0}{NH_m}; \frac{NH_0}{fL}, \frac{f}{N}\right), \tag{3.15a, b}$$

in terms of a new non-dimensional function F_2, where we wish to emphasize that only variations in the first argument are being considered at the moment. Now, unless U_0 is close to U_c, particles which are elevated to the horizontal plane at the top of the topographic feature are unaware of the total height of the feature. Thus (3.15) must be a relationship independent of h_m and hence of the form

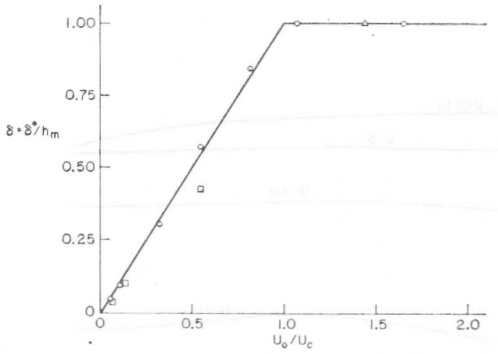

Fig. 12. The normalized maximum displacement of a fluid particle reaching the horizontal plane touching the top of the topographic feature of height △ 75 m, ○ 200 m and □ 800 m.

$$\delta = \frac{\delta^*}{h_m} = \frac{U_0}{Nh_m} F_3\left(\frac{NH_0}{fL}, \frac{f}{N}\right), \qquad (3.16a, b)$$

where F_3 is another non-dimensional function. Thus δ is a linear function of U_0 passing through the origin (zero flow implies zero displacement). Using the fact that $\delta = 1$ when $U = U_c$, we see that

$$F_3\left(\frac{NH_0}{fL}, \frac{f}{N}\right) = Nh_m/U_c, \qquad (3.17)$$

from which (3.13a) follows. We note that (3.17) is consistent with the fact that U_c is linearly proportional to h_m if all other quantities are held fixed and that the above argument indicates that (3.13) is correct for all NH_0/fL and f/N; the influence of these quantities and the shape of the feature is expressed in the value of U_c. The argument also indicates why (3.13) describes the $h_m = 200$ m results better than the $h_m = 800$ m results. HUPPERT's (1975) linearized boundary condition, zero Rossby number calculation for U_c is not entirely adequate for the higher feature at the Rossby number $U_c/fL \approx 0.2$. The inclusion of the influence of these two effects—the non-linearization of the lower boundary condition and finite Rossby number—would lead to an increased value of U_c. A 25% increase for $h_m = 800$ m leads to a very close agreement between the data and relationship (3.13a).

Another measure of the amplitude of the disturbance is the total perturbation potential energy over the entire volume. Compared to the maximum displacement at a single point, it provides a measure which is less sensitive to details of the patterns. The expression for potential energy is

$$\text{P.E.} = \frac{g^2}{\rho_0 N^2} \iiint (\rho - \bar{\rho})^2 \, dx \, dy \, dz, \qquad (3.18)$$

where the overbar indicates a horizontal average over the entire area. In Fig. 13a the normalized potential energy is plotted as a function of time for all the cases in which the height of the topographic feature is 200 m. In every case the potential energy rises abruptly, reaches a maximum value and then fluctuates on a time scale much longer than that required for the initiation of the disturbance. The time required for the disturbance to form is proportional to the advection time, L/U_0. The maximum values of the potential energy are plotted in Fig. 13b as a function of the energy of the incoming flow on a log–log scale. As might be anticipated from the results in Fig. 12 the potential energy is proportional to the energy of the incoming flow for $U_0 < U_c$ (Froude number less than unity). For larger values of the mean flow the potential energy increases, but only slightly with increasing energy of the mean flow. Specifically, a straight line fit to the calculated points, indicates an increase of potential energy by a 0.15 power of the energy of the incoming flow.

4. THE ANALYTIC MODEL

A number of aspects of the numerical results can be deduced from a rather simple mathematical model of the transient flow. The model is inviscid and non-diffusive and assumes the flow to be in geostrophic and hydrostatic balance. A general solution of the resulting equations of motion is obtained in terms of the (unknown) density distribution on the bottom boundary. Modelling this density distribution in accord with the ideas described in Section 2, we obtain a useful,

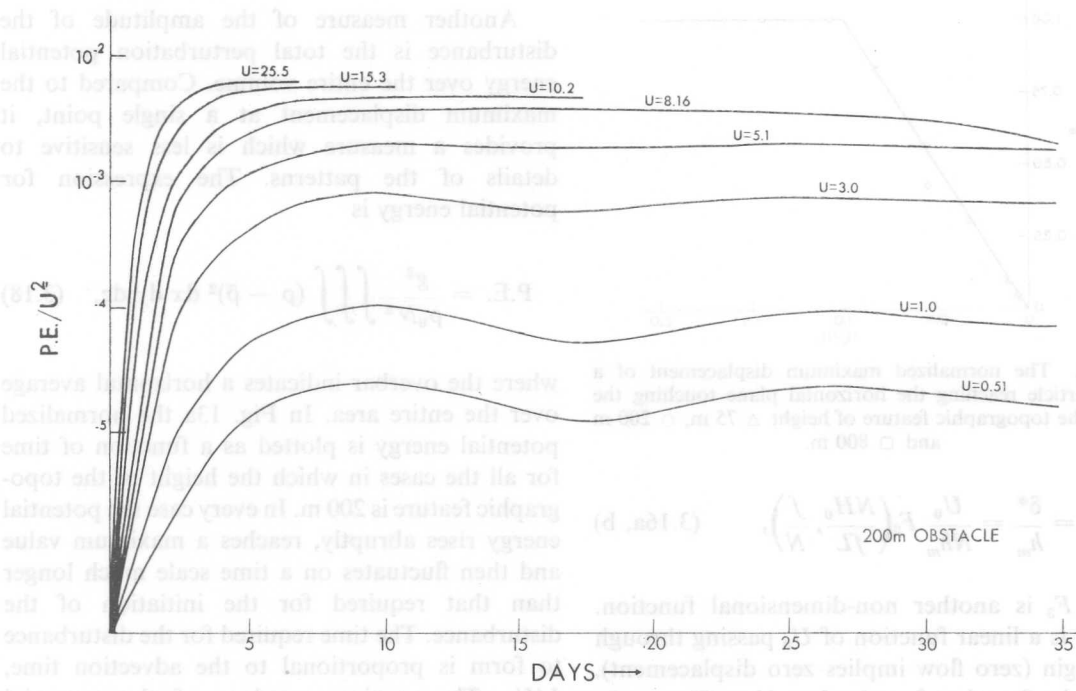

Fig. 13(a). The potential energy as a function of time for $h_m = 200$ m.

quantitative description of the transient flow. In particular, the parameter regime for which the shed cyclonic vorticity remains close to the isolated topographic feature is calculated.

Define σ, the perturbation buoyancy per unit mass, and π, the pressure minus its hydrostatic portion divided by the reference density ρ_0, so that

$$\rho = \rho_0 e^{-\beta z} + \rho_0 \sigma / g \tag{4.1}$$

and

$$p = -(\rho_0 g/\beta) e^{-\beta z} + \rho_0 \pi. \tag{4.2}$$

Then the quasi-geostrophic potential vorticity equation is

$$\frac{D}{Dt}\left[\nabla^2 \pi - \frac{f^2}{N^2}\,\partial_z \sigma\right] = 0, \tag{4.3}$$

and the hydrostatic relationship is

$$\partial_z \pi = -\sigma. \tag{4.4}$$

The substitution of (4.4) into (4.3) yields the relationship

$$\frac{D}{Dt}\left[\nabla^2 \pi + \frac{f^2}{N^2}\,\partial^2_{zz}\,\pi\right] = 0. \tag{4.5}$$

Since the quantity in square brackets is initially zero, it remains zero and the equation governing the motion is

$$\nabla^2 \pi + (f^2/N^2)\,\partial^2_{zz}\,\pi = 0. \tag{4.6}$$

The boundary conditions on π are determined by combining the density conservation equation

$$\frac{D\sigma}{Dt} - N^2 w = 0, \tag{4.7}$$

and the requirement of zero normal flow at the upper and lower boundaries,

$$w = 0 \qquad (z = 0) \tag{4.8}$$

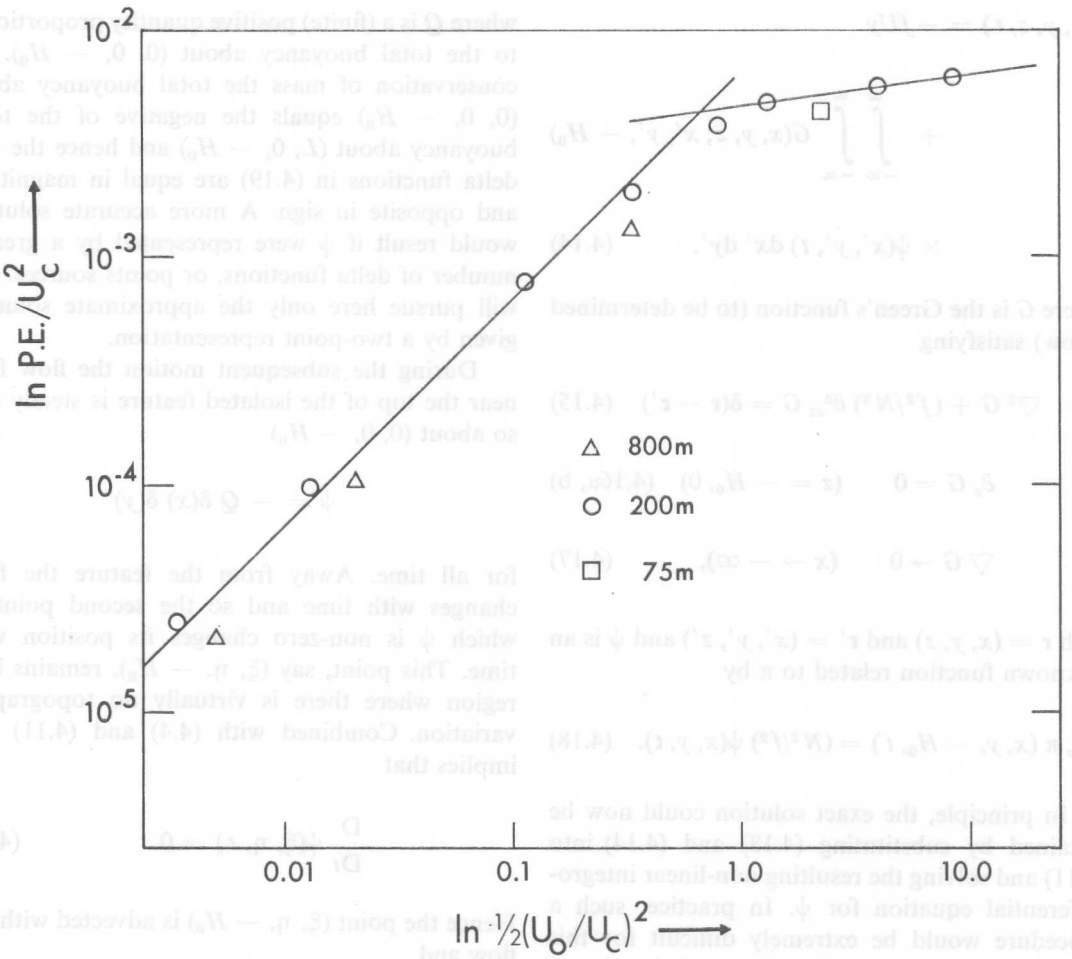

Fig. 13(b). The potential energy as a function of the velocity.

$$w = -\frac{DH}{Dt} \quad [z = -H(x, y)] \tag{4.9}$$

with (4.4) to yield

$$\frac{D}{Dt}\,\partial_z \pi = 0 \qquad (z = 0) \tag{4.10}$$

and

$$\frac{D}{Dt}\,(\partial_z \pi - N^2 H) = 0 \quad [z = -H(x, y)]. \tag{4.11}$$

The condition (4.10) can be integrated and the initial condition of π incorporated to yield

$$\partial_z \pi = 0 \quad (z = 0). \tag{4.12}$$

To these must be added the condition

$$\nabla \pi = -fU(0, 1) \quad (x \to -\infty), \tag{4.13}$$

which expresses the fact that far upstream there is a uniform flow in the x-direction of magnitude U.

The general solution of (4.6), (4.12) and (4.13) is

$$\pi(x, y, z, t) = -fUy + \int_{-\infty}^{\infty}\int_{-\infty}^{\infty} G(x, y, z; x', y', -H_0) \times \psi(x', y', t)\, dx'\, dy', \quad (4.14)$$

where G is the Green's function (to be determined below) satisfying

$$\nabla^2 G + (f^2/N^2)\,\partial^2_{zz} G = \delta(\mathbf{r} - \mathbf{r}') \quad (4.15)$$

$$\partial_z G = 0 \qquad (z = -H_0, 0) \quad (4.16a, b)$$

$$\nabla G \to 0 \qquad (x \to -\infty), \quad (4.17)$$

with $\mathbf{r} = (x, y, z)$ and $\mathbf{r}' = (x', y', z')$ and ψ is an unknown function related to π by

$$\partial_z \pi\,(x, y, -H_0, t) = (N^2/f^2)\,\psi(x, y, t). \quad (4.18)$$

In principle, the exact solution could now be obtained by substituting (4.18) and (4.14) into (4.11) and solving the resulting non-linear integro-differential equation for ψ. In practice, such a procedure would be extremely difficult for this time-dependent flow and lies beyond the aim of the model which is a simple determination of the overall properties of the flow. To this end we adopt an approximate representation for ψ, and thereby generalize to rotating stratified flows the idea of describing non-rotating homogeneous flows in terms of line vortices (BATCHELOR, 1967, Section 7.3). During the initial advection, relatively cold water is advected to the top of the isolated feature replacing warmer water which is advected downstream by a distance comparable to the length scale of the topography. Hence, at the end of this stage let ψ be everywhere zero except around the points $(0, 0, -H_0)$ and $(L, 0, -H_0)$ and expressable as

$$\psi(x, y, t) = Q\,[\delta(x - L) - \delta(x)]\,\delta(y), \quad (4.19)$$

where Q is a (finite) positive quantity proportional to the total buoyancy about $(0, 0, -H_0)$. By conservation of mass the total buoyancy about $(0, 0, -H_0)$ equals the negative of the total buoyancy about $(L, 0, -H_0)$ and hence the two delta functions in (4.19) are equal in magnitude and opposite in sign. A more accurate solution would result if ψ were represented by a greater number of delta functions, or points sources. We will pursue here only the approximate solution given by a two-point representation.

During the subsequent motion the flow field near the top of the isolated feature is steady and so about $(0, 0, -H_0)$

$$\psi = -Q\,\delta(x)\,\delta(y)$$

for all time. Away from the feature the flow changes with time and so the second point at which ψ is non-zero changes its position with time. This point, say $(\xi, \eta, -H_0)$, remains in a region where there is virtually no topographic variation. Combined with (4.4) and (4.11) this implies that

$$\frac{D}{Dt}\,\psi(\xi, \eta, t) = 0. \quad (4.20)$$

Hence the point $(\xi, \eta, -H_0)$ is advected with the flow and

$$\psi(x, y, t) = Q[\delta(x - \xi)\,\delta(y - \eta) - \delta(x)\,\delta(y)]. \quad (4.21)$$

Thus

$$\frac{d\xi}{dt} = U(\xi, \eta, -H_0, t) \quad (4.22a)$$

$$= -\frac{1}{f}\,\partial_\eta\,\pi\,(\xi, \eta, -H_0, t) \quad (4.22b)$$

$$= U - \frac{1}{f}\int_{-\infty}^{\infty}\int_{-\infty}^{\infty} \partial_\eta G(\xi, \eta, -H_0; x', y', -H_0) \times \psi(x', y', t)\, dx'\, dy' \quad (4.22c)$$

$$= U + (Q/f)\,\partial_\eta\, G_0(\xi, \eta), \quad (4.22d)$$

where

$$G_0(\xi, \eta) = G(\xi, \eta, -H_0; 0, 0, -H_0), \quad (4.23)$$

and the point $(x', y') = (\xi, \eta)$ makes no contribution to (4.22c) because $\partial_\eta G(\xi,\eta, -H_0; x'y', -H_0)$ is an odd function about $y' = \eta$, and $\delta(y' - \eta)$ is an even function. The physical interpretation of this fact is that the source point (ξ, η) moves under the combined influence of the upstream flow and the anticyclonic vorticity centred on $(0, 0, -H_0)$, but there is no self-induced motion. Analogously to (4.22), we write,

$$\frac{d\eta}{dt} = v(\xi, \eta, -H_0, t) \quad (4.24a)$$

$$= f^{-1}\,\partial_\xi\, \pi(\xi,\eta, -H_0, t) \quad (4.24b)$$

$$= \frac{1}{f}\int_{-\infty}^{\infty}\int_{-\infty}^{\infty} \partial_\xi\, G(\xi, \eta, -H_0; x', y', -H_0) \times \psi(x', y', t)\, dx'dy' \quad (4.24c)$$

$$= -(Q/f)\,\partial_\xi\, G_0(\xi, \eta). \quad (4.24d)$$

Dividing (4.24d) by (4.22d), we obtain

$$\frac{d\eta}{d\xi} = \frac{-Q\,\partial_\xi\, G_0(\xi, \eta)}{fU + Q\,\partial_\eta\, G_0(\xi, \eta)}. \quad (4.25)$$

To this equation we add the initial conditions

$$\xi = L, \quad \eta = 0, \quad (4.26)$$

which state that after the initial advection, the shed cyclonic vorticity is one length scale directly downstream of the top of the topographic feature. The solution of (4.25) and (4.26) is

$$fU\,\eta + Q\,G_0(\xi, \eta) = Q\,G_0(L, 0). \quad (4.27)$$

With the introduction of the non-dimensional horizontal coordinates (X, Y) by

$$(\xi, \eta) = L\,(X, Y), \quad (4.28)$$

(4.27) can be written in terms of the parameter γ as

$$\gamma Y + \mathscr{G}(X, Y) = \mathscr{G}(1, 0), \quad (4.29)$$

where

$$\gamma = 4\pi\, H_0\, fUL/Q \quad (4.30)$$

and

$$\mathscr{G}(X, Y) = 4\pi\, H_0\, G_0(\xi/L, \eta/L). \quad (4.31)$$

We now turn to the evaluation of Q, the total buoyancy induced over the topographic feature. This is done by comparing (4.18) and (4.19) with the boundary condition (4.11) yet to be satisfied and using the relationship (3.13). For $U_0 > U_c$, the buoyancy is due to particles whose vertical displacement is $h(x, y)$ and hence

$$Q = f^2 \int_{-\infty}^{\infty}\int_{-\infty}^{\infty} h(x, y)\, dx\, dy \quad (U_0 \geq U_c). \quad (4.32)$$

For the circularly symmetric features we are here considering it is convenient to reflect this in the expression for $h(x, y)$ by defining a function $m(r)$ of maximum value unity such that

$$h(x, y) = h_m\, m(r), \quad (4.33)$$

which will be assumed to be a monotonically decreasing function of r. This latter assumption is not necessary but it somewhat simplifies the analysis. Using (4.33), we can rewrite (4.32) as

$$Q = 2\pi f^2\, h_m \int_0^{\infty} rm(r)\, dr \quad (U_0 \geq U_c). \quad (4.34)$$

For $U_0 < U_c$, the buoyancy induced is due to

particles which have undergone a vertical displacement of at most $h_m\delta$. Thus the total buoyancy is reduced from that given by (4.34) by an amount

$$2\pi f^2 h_m \int_0^{r_0} r[m(r) - \delta]\, dr, \tag{4.35}$$

where $m(r_0) = \delta$. Subtracting (4.35) from (4.34), we obtain the relationship

$$Q = 2\pi f^2 h_m \left[\int_{r_0}^{\infty} rm(r)\, dr + \tfrac{1}{2} r_0^2 \delta\right] \quad (U_0 \leqslant U_c). \tag{4.36}$$

The physical interpretation of the upper limit r_0 in (4.34) is that for $r > r_0$, $m(r) < \delta$ and so particles are elevated by the full amount $h_m m(r)$ for $r > r_0$. Substituting the cylindrical gaussian (3.8) into (4.34) and (4.36) and using (3.13), we obtain

$$Q = \pi h_m f^2 L^2 \quad (U_0 \geq U_c) \tag{4.37a}$$

$$= \pi h_m f^2 L^2 (U_0/U_c)[1 - \ln (U_0/U_c)] \quad (U_0 \leq U_c) \tag{4.37b}$$

Inserting (4.37) into (4.30), we obtain the final expression

$$\gamma = \frac{4H_0}{h_m f L} \begin{cases} U_0 & (U_0 \geq U_c) \quad (4.38a) \\ U_c/[1 - \ln (U_0/U_c)] & (U_0 \leq U_c), \quad (4.38b) \end{cases}$$

which is graphed in Fig. 14.

Expressions for $\mathscr{G}(X, Y)$ are determined in the Appendix, where it is shown that

$$\mathscr{G}(X, Y) = \ln (X^2 + Y^2) - 4 \sum_{n=1}^{\infty} K_0 [n\pi (X^2 + Y^2)^{\frac{1}{2}}/B] \tag{4.39}$$

$$\sim \ln (X^2 + Y^2) \quad (B \to 0) \tag{4.40a}$$

$$\sim -2B(X^2 + Y^2)^{-\frac{1}{2}} \quad (B \to \infty), \tag{4.40b}$$

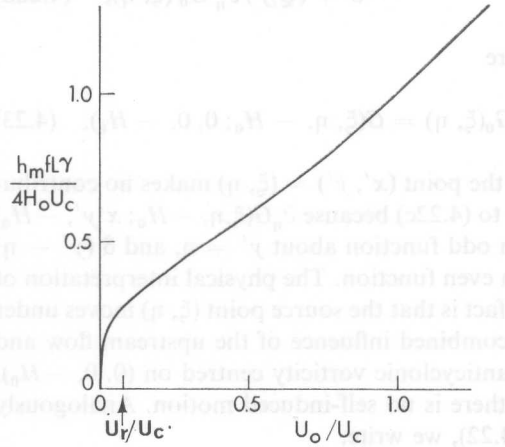

Fig. 14. A graph of the parameter γ as a function of U_0 as given by (4.38). Marked on the abscissa is the value of U_0 below which the analytic model predicts that the shed eddy remains in the vicinity of the topographic feature.

where

$$B = NH_0/fL. \tag{4.41}$$

Consider first the limit $B \to 0$, which corresponds to homogeneous flow. Then using (4.40a), we can write (4.29) as

$$X^2 + Y^2 = e^{-\gamma Y} \tag{4.42}$$

The family of curves (4.42) is presented in Fig. 15a for various values of γ. With some elementary calculus it can be shown that for $\gamma < 2e^{-1} \simeq 0.736$ the curves are closed and the free, cyclonic vorticity distribution remains close to the isolated feature. For $\gamma > 2e^{-1}$ the cyclonic vorticity distribution escapes, moving ever downstream. For this homogeneous situation the expression (4.34) can be obtained directly by modelling the flow by line vortices.

In the limit $B \to \infty$, (4.28) becomes

$$[\tfrac{1}{2}(\gamma/B)\, Y + 1]\,(X^2 + Y^2)^{\frac{1}{2}} = 1, \tag{4.43}$$

a relationship which is plotted for various values of (γ/B) in Fig. 15b. For $\gamma < 1/2B$ the curves

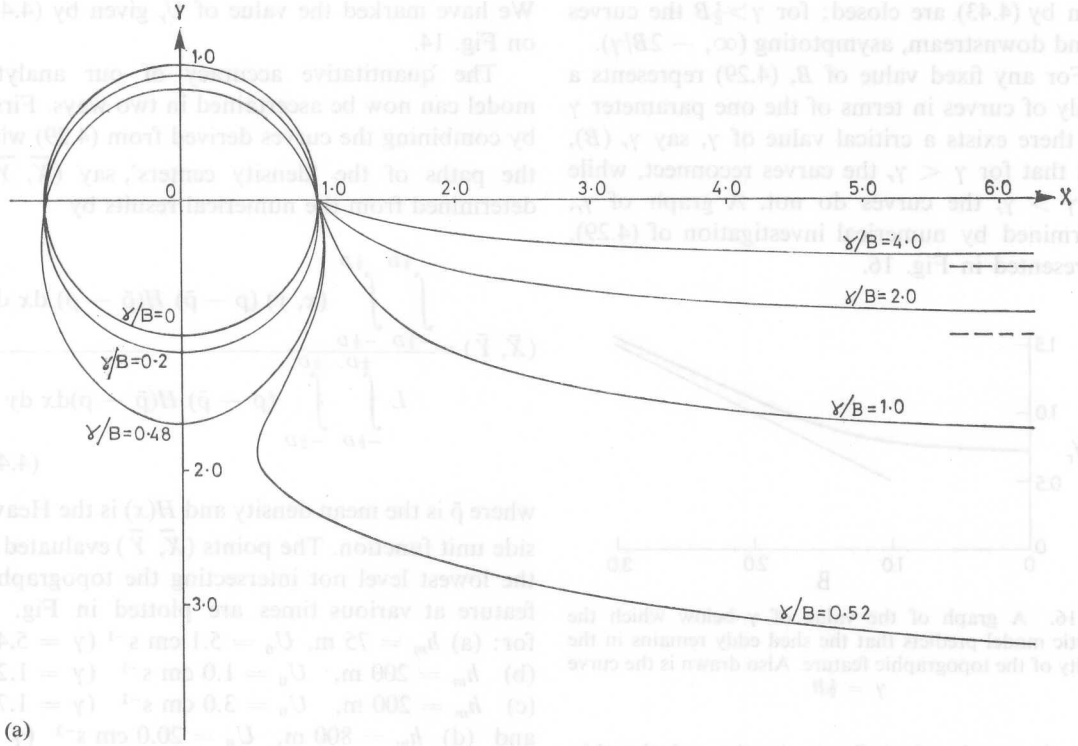

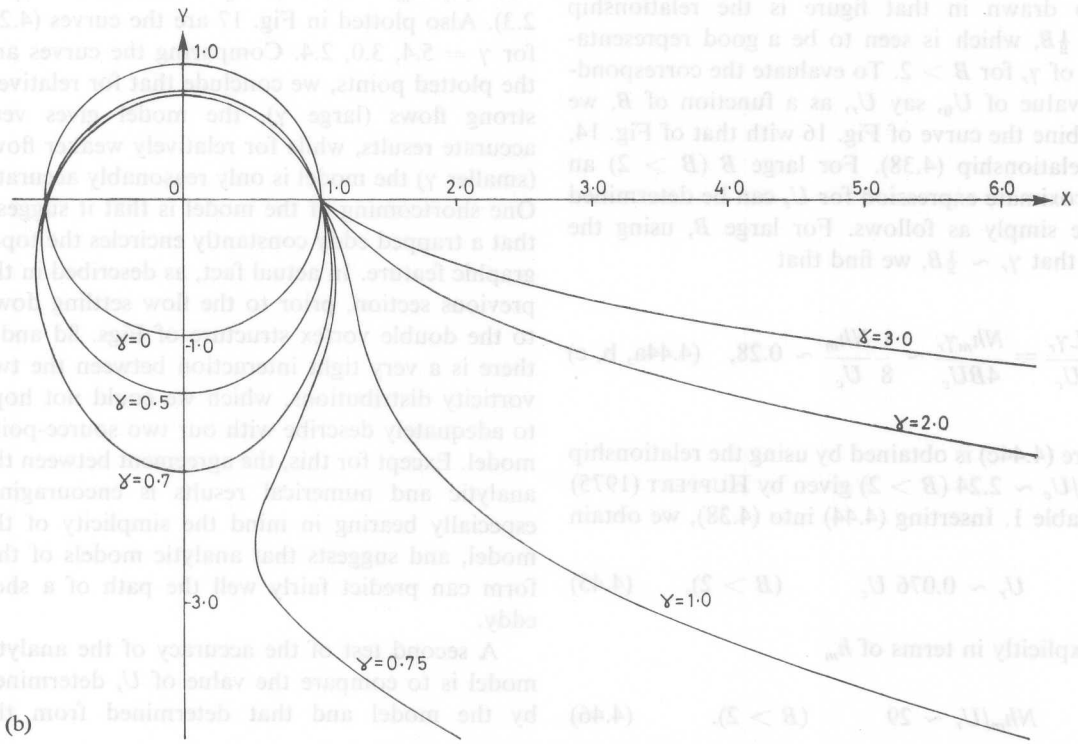

Fig. 15. The paths of the cyclonic point source as given by (4.29). (a) In the limit $B = 0$, equation (4.42), and (b) in the limit $B = \infty$, equation (4.43).

given by (4.43) are closed; for $\gamma > \frac{1}{2}B$ the curves extend downstream, asymptoting $(\infty, -2B/\gamma)$.

For any fixed value of B, (4.29) represents a family of curves in terms of the one parameter γ and there exists a critical value of γ, say γ_r (B), such that for $\gamma < \gamma_r$ the curves reconnect, while for $\gamma > \gamma_r$ the curves do not. A graph of γ_r, determined by numerical investigation of (4.29), is presented in Fig. 16.

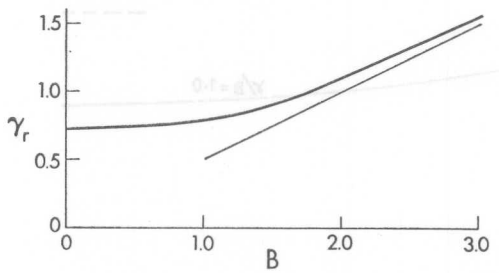

Fig. 16. A graph of the value of γ below which the analytic model predicts that the shed eddy remains in the vicinity of the topographic feature. Also drawn is the curve $\gamma = \frac{1}{2}B$.

Also drawn in that figure is the relationship $\gamma = \frac{1}{2}B$, which is seen to be a good representation of γ_r for $B > 2$. To evaluate the corresponding value of U_0, say U_r, as a function of B, we combine the curve of Fig. 16 with that of Fig. 14, or relationship (4.38). For large B $(B > 2)$ an approximate expression for U_r can be determined quite simply as follows. For large B, using the fact that $\gamma_r \sim \frac{1}{2}B$, we find that

$$\frac{h_m f L \gamma_r}{4 H_0 U_c} = \frac{N h_m \gamma_r}{4 B U_c} \sim \frac{1}{8}\frac{N h_m}{U_c} \sim 0.28, \quad \text{(4.44a, b, c)}$$

where (4.44c) is obtained by using the relationship $Nh_m/U_c \sim 2.24$ $(B > 2)$ given by HUPPERT (1975) in Table 1. Inserting (4.44) into (4.38), we obtain

$$U_r \sim 0.076\, U_c \qquad (B > 2), \qquad (4.45)$$

or explicitly in terms of h_m

$$N h_m / U_r \sim 29 \qquad (B > 2). \qquad (4.46)$$

We have marked the value of U_r given by (4.45) on Fig. 14.

The quantitative accuracy of our analytic model can now be ascertained in two ways. First, by combining the curves derived from (4.29) with the paths of the 'density centers', say $(\bar{X}, \bar{Y})$, determined from the numerical results by

$$(\bar{X}, \bar{Y}) = \frac{\int_{-\frac{1}{2}D}^{\frac{1}{2}D}\int_{-\frac{1}{2}D}^{\frac{1}{2}D} (x, y)\,(\rho - \bar{\rho})\, H(\bar{\rho} - \rho)\, dx\, dy}{L \int_{-\frac{1}{2}D}^{\frac{1}{2}D}\int_{-\frac{1}{2}D}^{\frac{1}{2}D} (\rho - \bar{\rho})\, H(\bar{\rho} - \rho) dx\, dy} \qquad (4.47)$$

where $\bar{\rho}$ is the mean density and $H(x)$ is the Heaviside unit function. The points $(\bar{X}, \bar{Y})$ evaluated at the lowest level not intersecting the topographic feature at various times are plotted in Fig. 17 for: (a) $h_m = 75$ m, $U_0 = 5.1$ cm s^{-1} $(\gamma = 5.4)$; (b) $h_m = 200$ m, $U_0 = 1.0$ cm s^{-1} $(\gamma = 1.2)$; (c) $h_m = 200$ m, $U_0 = 3.0$ cm s^{-1} $(\gamma = 1.7)$; and (d) $h_m = 800$ m, $U_0 = 20.0$ cm s^{-1} $(\gamma = 2.3)$. Also plotted in Fig. 17 are the curves (4.29) for $\gamma = 5.4, 3.0, 2.4$. Comparing the curves and the plotted points, we conclude that for relatively strong flows (large γ), the model gives very accurate results, while for relatively weaker flows (smaller γ) the model is only reasonably accurate. One shortcoming of the model is that it suggests that a trapped eddy constantly encircles the topographic feature. In actual fact, as described in the previous section, prior to the flow settling down to the double vortex structure of Figs. 8d and e there is a very tight interaction between the two vorticity distributions, which we could not hope to adequately describe with our two source-point model. Except for this, the agreement between the analytic and numerical results is encouraging, especially bearing in mind the simplicity of the model, and suggests that analytic models of this form can predict fairly well the path of a shed eddy.

A second test of the accuracy of the analytic model is to compare the value of U_r determined by the model and that determined from the

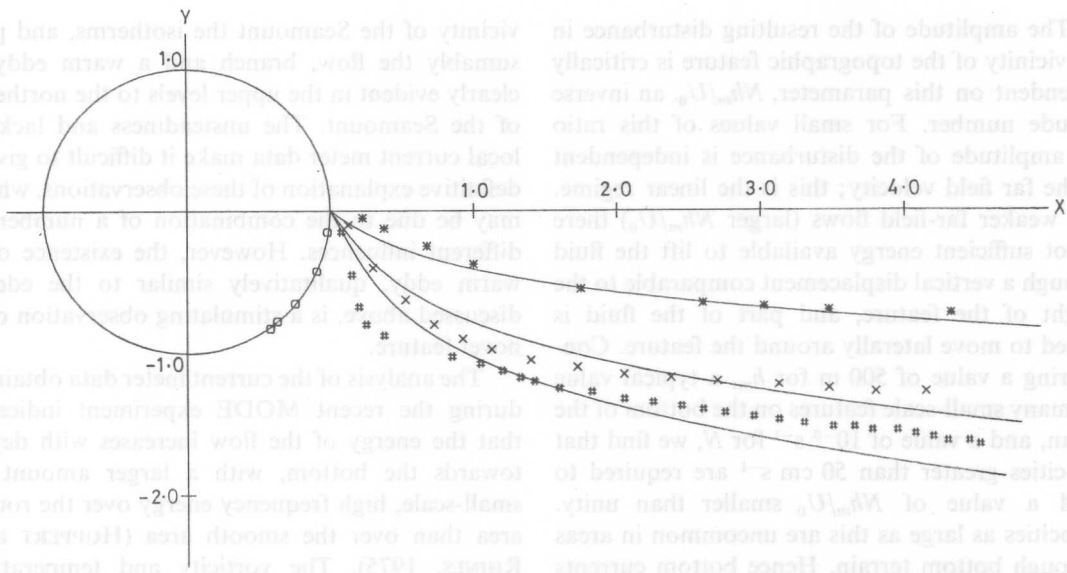

Fig. 17. The paths of the cyclonic point source as given by (4.29) for $B = 2$ and $\gamma = 5.4$, 3.0, and 2.4. Also plotted are the density centers of the cyclonic eddy: $*U_0 = 5.1$ cm s^{-1}, $h_m = 75$ m; $\times$ $U_0 = 20.0$ cm s^{-1}, $h_m = 800$ m; $\#$ $U_0 = 3.0$ cm s^{-1}, $h_m = 200$ m; and $+$ $U_0 = 1.0$ cm s^{-1}, $h_m = 200$ m.

numerical calculations. This would require quite a large amount of calculation and we have not carefully carried out such a test. The only such comparison possible with the computations we have carried out is for $h_m = 200$ m, for which the analysis predicts that $U_r = 0.9$ while our numerical calculations indicate that $1.0 < U_r < 3.0$. By inspection of the flow patterns for $U_0 = 1.0$ and 3.0 it would appear that U_r is much closer to 1.0 than 3.0. Thus, again, the conclusion is that there is reasonable agreement between the analytical and numerical results.

A useful, order-of-magnitude conclusion might be stated as follows. For large values of B, if NR_m/U_0 is greater than a number of order unity, a Taylor column is formed above the topographic feature and if Nh_m/U_0 is greater than a number of order ten, the shed eddy, generated by the initiation process, remains in the vicinity of the topographic feature.

5. CONCLUSIONS AND OCEANOGRAPHIC IMPLICATIONS

From our investigation of the interaction of a temporally varying mean flow with an isolated topographic feature, we can deduce the following general statements. Mean flow variations cause vorticity redistribution with anticyclonic vorticity regions over the topographic feature and cyclonic vorticity regions shed from the feature. Associated with these vorticity regions are anomalous temperature regions. Both the cold anomaly, which corresponds to the anticyclonic vorticity distribution, and the warm anomaly, which corresponds to the cyclonic vorticity distribution, are evidenced by closed isopycnal contours. The cold anomaly remains trapped over the topographic feature, while the shed warm anomaly drifts off downstream for sufficiently large mean flow velocities. For weaker mean flows, the shed warm anomaly remains in the vicinity of the topographic feature, leading to a double vortex structure. The shed temperature anomaly can be described as an eddy and our investigation hence suggests a mechanism for the generation of eddies beneath the main thermocline. Such eddies can be generated whenever the mean flow changes in such a way that the vorticity, or density, in the vicinity of the topographic feature is redistributed, a situation which we have shown occurs if Nh_m/U_0 is larger than a number of order unity.

The amplitude of the resulting disturbance in the vicinity of the topographic feature is critically dependent on this parameter, Nh_m/U_0, an inverse Froude number. For small values of this ratio the amplitude of the disturbance is independent of the far field velocity; this is the linear regime. For weaker far-field flows (larger Nh_m/U_0) there is not sufficient energy available to lift the fluid through a vertical displacement comparable to the height of the feature, and part of the fluid is forced to move laterally around the feature. Considering a value of 500 m for h_m, a typical value for many small-scale features on the bottom of the ocean, and a value of 10^{-3} s^{-1} for N, we find that velocities greater than 50 cm s^{-1} are required to yield a value of Nh_m/U_0 smaller than unity. Velocities as large as this are uncommon in areas of rough bottom terrain. Hence bottom currents are subcritical in this sense and a predominant part of the flow will be around rather than over the bottom features.

These ideas can be used to explain some aspects of a recent study in the New England Sea Mount Chain (VASTANO and WARREN, 1976). On a Woods Hole Oceanographic Institution cruise during mid-1971, Vastano and Warren made a series of XBT observations and regularly spaced (*ca.* 20 km) STD stations around the Atlantis II Seamount, which is roughly circularly symmetric with a 'radius' of approximately 15 km at 4000 m, rising to a summit of 1645 m from an ocean floor at a depth of 5000 m. The Seamount is in the vicinity of the Gulf Stream and Vastano and Warren report that the stream at that time was varying so rapidly that they obtained a coherent synoptic picture of the flow for only one 5-day period. During this time the potential temperature maps at 3500, 3000, 2500 and 2000 m indicate that the flow was fairly steady and in a direction which varied from level to level between eastward and northeastward. The maps at 1500 and 2500 m containing the individual stations and Vastano and Warren's interpolated temperature contours are reproduced in Fig. 18; for the maps at other depths and a more complete description of the experiment than we give here we refer the reader to Vastano and Warren's paper. In the vicinity of the Seamount the isotherms, and presumably the flow, branch and a warm eddy is clearly evident in the upper levels to the northeast of the Seamount. The unsteadiness and lack of local current meter data make it difficult to give a definitive explanation of these observations, which may be due to the combination of a number of different influences. However, the existence of a warm eddy, qualitatively similar to the eddies discussed above, is a stimulating observation of a novel feature.

The analysis of the current meter data obtained during the recent MODE experiment indicates that the energy of the flow increases with depth towards the bottom, with a larger amount of small-scale, high frequency energy over the rough area than over the smooth area (HUPPERT and RHINES, 1975). The vorticity and temperature redistribution mechanism we have discussed could contribute to this energy increase. An interesting feature of the IOS (Institute of Oceanographic Sciences) float tracks in MODE is the existence of a hook-shaped trajectory at one end of a topographic knoll (Gould, private communication). Such a track is consistent with the flow field induced by two closely spaced vorticity distributions of opposite signs, of the nature described as case *S* of Section 3.

The concept of vorticity redistribution by the interaction of varying mean flows with topography may also be important in the atmosphere. Cyclogenesis is well known to occur in the lee of the large mountain ranges, though the mechanism of its occurrence is not understood. In a recent numerical simulation of the global circulation of the atmosphere, MANABE and TERPSTRA (1974) specifically studied the initiation of cyclones. They found that a model including the large mountain ranges of the Earth predicted the distribution and frequency of cyclogenesis in much better agreement with that observed in the actual atmosphere than did a model without mountains. The cyclogenesis in both model and atmosphere occurs predominantly in the South China Sea in the lee of the Tibetan Plateau and in the southeastern United States in the lee of the Rocky Mountains. Manabe and Terpstra speculate (their word) that

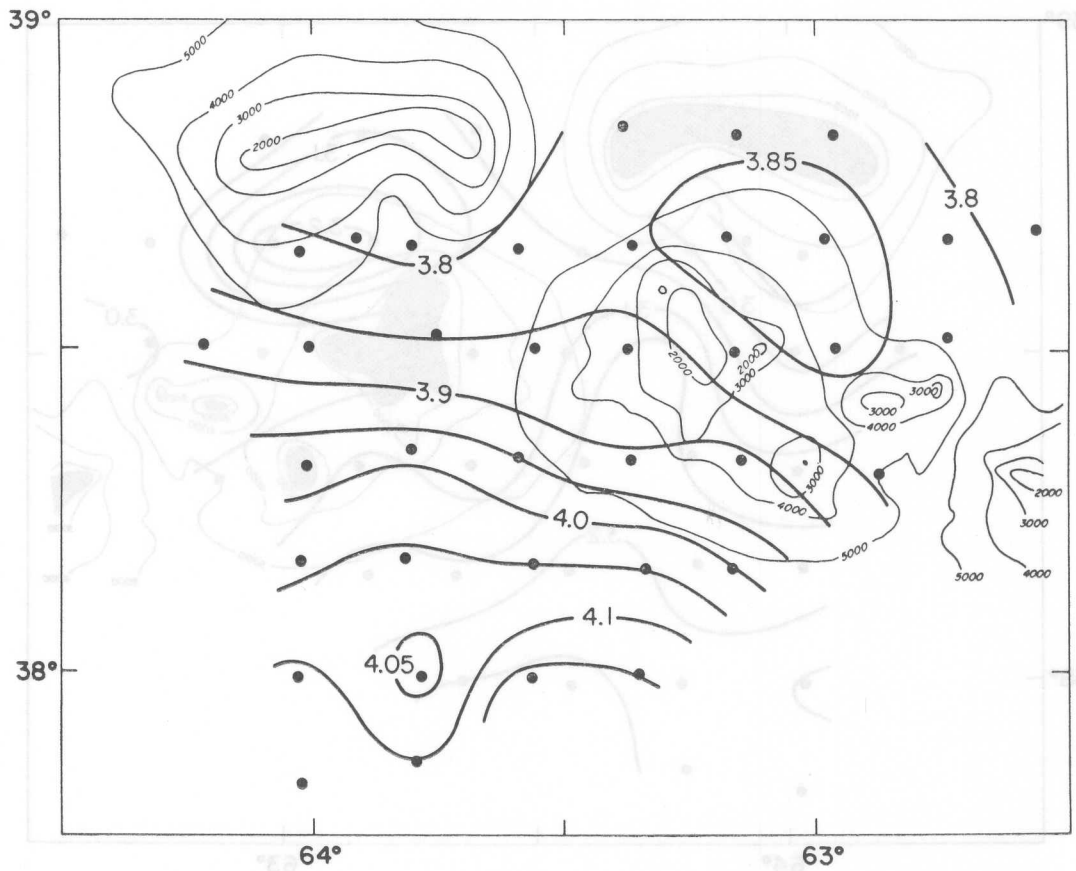

Fig. 18(a). The STD stations of Vastano and Warren in the vicinity of the Atlantis II Seamount at 1500 m.

cyclogenesis may be due to baroclinic instability in the intensified jet stream over these areas or it may be due to the influence of the mountains in modifying the airmass distribution. We suggest that temporal variations in the jet stream over mountainous regions lead to continual redistribution of the vorticity pattern and the shedding of cyclonic vorticity which organizes in such a way that the occurrence of cyclones is facilitated. At present, this explanation is, like all others that have been applied to this fundamental problem, a possibility that requires further consideration.

Much further work is suggested by our present investigation. We plan in the future to consider the effects of vertical shear, beta and the interaction of an eddy with another topographic feature, to mention only a few possible extensions of our present efforts. Finally, there are a large number of different regions in both the oceans and atmosphere where we would like to see these ideas applied and compared with observations.

Acknowledgements—We thank Mr. L. Lewis of GFDL who helped carry out most of the computations reported in this paper. Assistance with some numerical aspects was also given to us by Dr. Joyce Wheeler of DAMTP. The work benefitted from stimulating discussions with Dr. P. B. Rhines, Dr. S. Manabe and Dr. B. Warren who kindly showed us prior to publication the data taken by Dr. A. Vastano and himself. The paper was written while HEH was visiting the Department of Earth and Planetary Sciences at M.I.T. He thanks the members of that department, and in particular Professor C. I. Wunsch, who helped arrange the visit, for their generous hospitality during this time. A majority of the computations were performed at the Geophysical Fluid Dynamics Laboratory

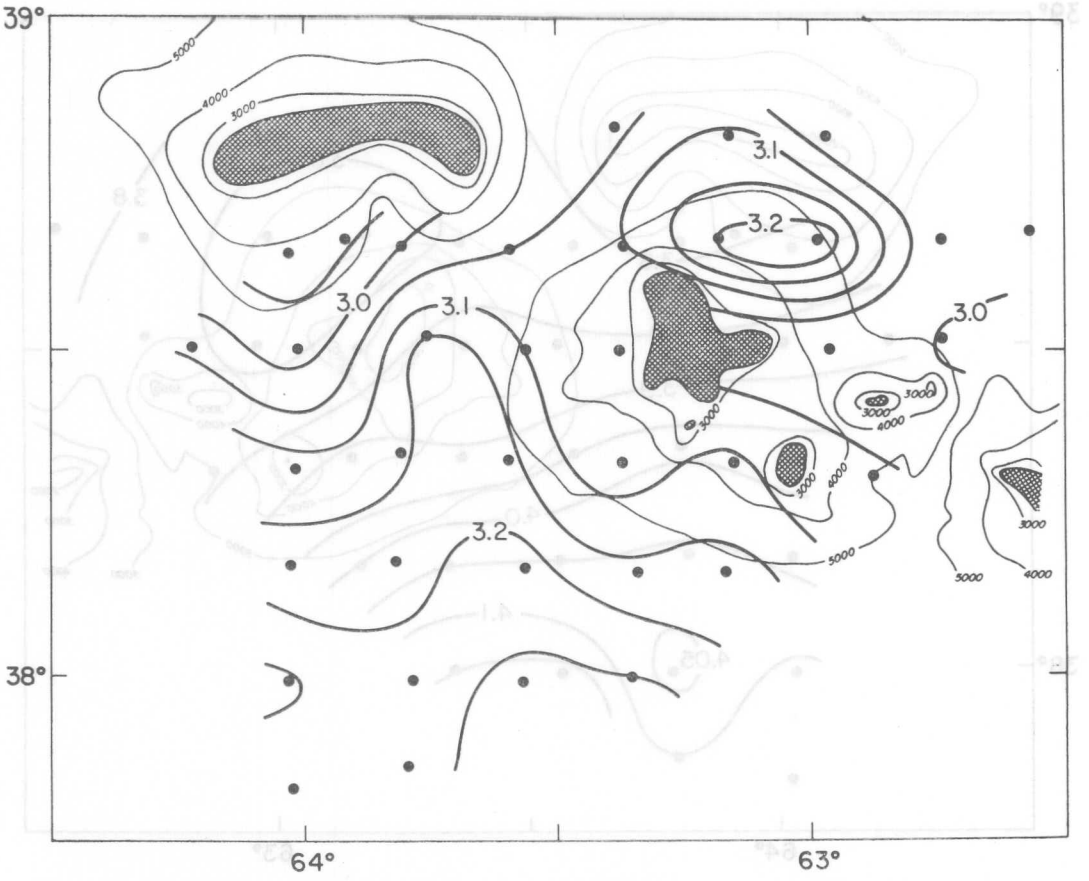

Fig. 18b. The STD stations of Vastano and Warren in the vicinity of the Atlantis II Seamount at 2500 m.

of NOAA and the work was supported by grants from the British Admiralty and by grant number IDO74-24095 from the International Decade of Ocean Exploration Office of the National Science Foundation through M.I.T.

REFERENCES

BATCHELOR G. K. (1967) *An introduction to fluid dynamics*, Cambridge University Press, 615 pp.

BRETHERTON F. P. (1975) Recent developments in dynamical oceanography. *Quarterly Journal of the Royal Meteorological Society*, **101**, 705–721.

BRYAN K. (1969) A numerical method for the study of the circulation of the world ocean. *Journal of Computational Physics*, **4**, 347–376.

CREASE J. (1962) Velocity measurements in the deep water of the western North Atlantic. *Journal of Geophysical Research*, **67**, 3173–3176.

DRAZIN P. G. (1961) On the steady flow of a fluid of variable density past an obstacle. *Tellus*, **13**, 239–251.

GILL A. E., J. S. A. GREEN and A. J. SIMMONS (1974) Energy partition in the large-scale ocean circulation and the production of mid-ocean eddies. *Deep-Sea Research*, **21**, 499–528.

HOGG N. G. (1973) On the stratified Taylor column, *Journal of Fluid Mechanics*, **58**, 517–537.

HUPPERT H. E. (1975) Some remarks on the initiation of inertial Taylor columns. *Journal of Fluid Mechanics*, **67**, 397–412.

HUPPERT H. E. and P. B. RHINES (1975) Topographic dynamics. In: *Dynamics and the analysis of MODE* I, pp. 189–250.

MANABE S. and T. B. TERPSTRA (1974) The effects of mountains on the general circulation of the atmosphere as identified by numerical experiments. *Journal of Atmospheric Sciences*, **31**, 3–42.

PARKER C. E. (1971) Gulf Stream rings in the Sargasso Sea. *Deep-Sea Research*, **18**, 981–993.

RHINES P. B. (1975) Waves and turbulence on a beta-plane. *Journal of Fluid Mechanics*, **69**, 417–444.

ROBINSON A. R. and J. MCWILLIAMS (1974) Baroclinic instability in the open ocean. *Journal of Physical Oceanography*, **4**, 281–294.

STOMMEL H. (1955) Direct measurements of subsurface currents. *Deep-Sea Research*, **2**, 284–285.

SWALLOW J. C. (1971) The *Aries* current measurements in the western North Atlantic. *Philosophical Transactions of the Royal Society*, **A270**, 451–460.
SWALLOW J. C. and B. V. HAMON (1960) Some measurements of deep currents in the eastern North Atlantic. *Deep-Sea Research*, **6**, 155–168.
VASTANO A. C. and B. A. WARREN (1976) Perturbations to the Gulf Stream by Atlantis II Seamount. *Deep-Sea Research*, **23**, 681–694.
WEATHERLY G. L. (1972) A study of the bottom boundary layer of the Florida Current. *Journal of Physical Oceanography*, **2**, 54–72.

APPENDIX

The Green's function $G(x, y, z; x', y', z')$ is defined to satisfy (4.15) to (4.17). We seek the function $G(x, y, z; 0, 0, -H_0)$ which exhibits circular symmetry and can hence be expressed as $G_1(s, z)$, where

$$s = (x^2 + y^2)^{1/2}.$$

$G_1(s, z)$ satisfies

$$s^{-1}\,\partial_s\,(s\,\partial_s\,G_1) + (f^2/N^2)\,\partial^2_{zz}\,G_1 = (2\pi s)^{-1}\,\delta(s)\,\delta(z + H_0) \tag{A1}$$

$$\partial_z\,G_1 = 0 \qquad (z = -H_0, 0) \tag{A2a, b}$$

$$\nabla\,G_1 \to 0 \qquad (s \to \infty). \tag{A3}$$

In view of (A2), we express $G_1(s, z)$ and $\delta(z + H_0)$ as a cosine series in z by

$$G_1(s, z) = \tfrac{1}{2}g_0(s) + \sum_{n=1}^{\infty} g_n(s)\cos(n\pi z/H_0) \tag{A4}$$

and

$$\delta(z + H_0) = H_0^{-1} + 2H_0^{-1}\sum_{n=1}^{\infty}(-)^n\cos(n\pi z/H_0), \tag{A5}$$

where

$$g_n(s) = 2H_0^{-1}\int_{-H_0}^{0} G_1(s, z)\cos(n\pi z/H_0)\,\mathrm{d}z. \tag{A6}$$

Substituting (A4) and (A5) into (A1) and (A3), we obtain

$$s^{-1}\,\partial_s\,(s^{-1}\,\partial_s\,g_n) - (\pi^2\,n^2\,f^2/N^2\,H_0^2)\,g_n = (-)^n\,\delta(s)\,/\,(\pi H_0 s) \tag{A7}$$

$$\partial_s\,g_n \to 0 \quad (s \to \infty). \tag{A8}$$

The solution of (A7) and (A8) is

$$g_0 = (\pi\,H_0)^{-1}\ln(s/L) \tag{A9}$$

and

$$g_n = (-)^{n+1}(\pi H_0)^{-1}\,K_0(\pi nfs/NH_0) \quad (n = 1, 2, \ldots), \tag{A10}$$

where the length scale L appearing in (A9) is an arbitrary constant of integration. Substituting (A9) and (A10) into (A4), we obtain $G_1(s, z)$ and in particular

$$G_1(s, -H_0) = [\ln(s/L) - 2\sum_{n=1}^{\infty} K_0(\pi nfs/NH_0)]/(2\pi H_0). \tag{A11}$$

Introducing the non-dimensional radius r by $s = Lr$, we obtain

$$G_1(Lr, -H_0) = [\ln r - 2\sum_{n=1}^{\infty} K_0(\pi nr/B)]/(2\pi H_0), \tag{A12}$$

where

$$B = NH_0/fL. \tag{A13}$$

For small values of B, each term in the sum in (A12) is exponentially small and thus

$$G_1(Lr, -H_0) = \frac{1}{2\pi H_0}\ln r + \mathrm{O}(B^{-1/2}\mathrm{e}^{-\pi r/B}) \quad (B \to 0). \tag{A14}$$

For large values of B, using the Euler–Maclauren summation formula, we express $G_1(Lr, -H_0)$ as

$$G_1(Lr, -H_0) = [\ln r - \frac{2B}{\pi r}\int_{\pi r/B}^{\infty} K_0(t)\mathrm{d}t - K_0(\pi r/B) + 2\sum_{n=1}^{\infty}\frac{B_{2n}}{(2n)!}(\pi r/B)^{2n-1}\,K_0^{(2n-1)}(\pi r/B)]/2\pi H_0 \tag{A15}$$

$$= -\frac{B}{2\pi\,H_0}\,r^{-1} + \frac{1}{2\pi\,H_0}\ln B + \frac{0.129}{H_0} + \mathrm{O}(B^{-2}\ln B) \quad (B \to \infty). \tag{A16}$$

SWALLOW J. C. (1971) The Aiver current measurements in the western North Atlantic. Philosophical Transactions of the Royal Society, A270, 451–460.
SWALLOW J. C. and B. V. HAMON (1965) Some measurements of deep currents in the eastern North Atlantic. Deep-Sea Research, 6, 155–168.
VASTANO A. C. and B. A. WARREN (1976) Perturbations to the Gulf Stream by Atlantis II Seamount. Deep-Sea Research, 23, 681–694.
WUNSCH C. I. (1972) A study of the bottom boundary layer of the Florida Current. Journal of Physical Oceanography, 2, 54–72.

APPENDIX

The Green's function $G(x, y, z; x', y', z')$ is defined to satisfy (4.15) to (4.17). We seek the function $G(x, y, z; 0, 0, -H_0)$ which exhibits circular symmetry and can hence be expressed as $G_1(r, z)$, where

$$r = (x^2 + y^2)^{1/2}.$$

$G_1(r, z)$ satisfies

$$\nabla^2 G_1 + (f^2/N^2)\, f''_{zz}\, G_1 = (2\pi r)^{-1}\, \delta(r)\, \delta(z + H_0) \tag{A1}$$

$$f'_z\, G_1 = 0 \qquad (z = -H_0,\ 0) \tag{A2a, b}$$

$$\nabla\, G_1 \to 0 \qquad (r \to \infty). \tag{A3}$$

In view of (A2), we express $G_1(r, z)$ and $\delta(z + H_0)$ as a cosine series in z by

$$G_1(r, z) = \tfrac{1}{2} a_0(r) + \sum_{n=1}^{\infty} a_n(r) \cos(n\pi z/H_0) \tag{A4}$$

and

$$\delta(z + H_0) = H_0^{-1} + 2H_0^{-1} \sum_{n=1}^{\infty} (-)^n \cos(n\pi z/H_0). \tag{A5}$$

where

$$a_n(r) = 2H_0^{-1} \int_{-H_0}^{0} G_1(r, z) \cos(n\pi z/H_0)\, dz. \tag{A6}$$

Substituting (A4) and (A5) into (A1) and (A3), we obtain

$$r^{-1} f'_r (r f'_r a'_n) - (n^2 \pi^2 f^2/N^2 H_0^2)\, a_n$$

$$= (-)^n\, \delta(r)/(\pi H_0) \tag{A7}$$

$$a_n \to 0 \qquad (r \to \infty). \tag{A8}$$

The solution of (A7) and (A8) is

$$a_n = (\pi\, H_0)^{-1} \ln(r/L) \tag{A9}$$

and

$$a_n = (-)^n\, (\pi H_0)^{-1}\, K_0(n\pi r/H_0) \qquad (n = 1, 2, \ldots), \tag{A10}$$

where the length scale L appearing in (A9) is an arbitrary constant of integration. Substituting (A9) and (A10) into (A4), we obtain $G_1(r, z)$ and in particular

$$G_1(r, -H_0) = [\ln(r/L) - 2 \sum_{n=1}^{\infty} K_0(n\pi r/H_0)]/(2\pi H_0). \tag{A11}$$

Introducing the non-dimensional radius ν by $\nu = |r/L$, we obtain

$$G_1(L\nu, -H_0) = [\ln \nu - 2 \sum_{n=1}^{\infty} K_0(n\nu/\beta)]/(2\pi H_0), \tag{A12}$$

where

$$\beta = N H_0/f L. \tag{A13}$$

For small values of β, each term in the sum in (A12) is exponentially small and thus

$$G_1(L\nu, -H_0) = \frac{1}{2\pi H_0} \ln \nu + O(\beta^{-1} e^{-\pi/\beta}) \qquad (\beta \to 0). \tag{A14}$$

For large values of β, using the Euler–Maclaurin summation formula, we express $G_1(L\nu, -H_0)$ as

$$G_1(L\nu, -H_0) = [\ln \nu - \frac{2\beta}{\pi} \int_{\pi/\beta}^{\infty} K_0(t)\, dt - K_0(\pi/\beta)$$

$$+ 2 \sum_{n=1}^{\infty} \frac{B_{2n}}{(2n)!} (\pi/\beta)^{2n-1}\, K_0^{(2n-1)}(\pi/\beta)]/2\pi H_0 \tag{A15}$$

$$= -\frac{\beta}{2\pi H_0} e^{-\pi/\beta} + \frac{1}{2\pi H_0} \ln \beta + \frac{0.129}{H_0}$$

$$+ O(\beta^{-2} \ln \beta) \qquad (\beta \to \infty). \tag{A16}$$